Geoderma 401 (2021) 115330

Contents lists available at ScienceDirect

Geoderma

journal homepage: www.elsevier.com/locate/geoderma

Evaluation of soil thermal conductivity schemes incorporated into CLM5.0 in permafrost regions on the Tibetan Plateau

Shuhua Yang [a,b], Ren Li [a,*], Tonghua Wu [a,c], Xiaodong Wu [a], Lin Zhao [d], Guojie Hu [a], Xiaofan Zhu [a], Yizhen Du [a,b], Yao Xiao [a], Yuxin Zhang [a,b], Junjie Ma [a,b], Erji Du [a,b], Jianzong Shi [a], Yongping Qiao [a]

[a] Cryosphere Research Station on the Qinghai-Tibet Plateau, State Key Laboratory of Cryospheric Science, Northwest Institute of Eco-Environment and Resource, Chinese Academy of Sciences, Lanzhou, Gansu 730000, China
[b] University of Chinese Academy of Sciences, Beijing 100049, China
[c] Southern Marine Science and Engineering Guangdong Laboratory, Guangzhou 511458, China
[d] School of Geographical Sciences, Nanjing University of Information Science and Technology, Nanjing 210044, China

ARTICLE INFO

Handling Editor: Morgan Cristine L.S.

Keywords:
Soil thermal conductivity
Soil temperature
CLM
Permafrost
Tibetan Plateau

ABSTRACT

Soil thermal conductivity (STC) is essential parameter for revealing thermodynamic changes and projecting changes in soil thermal regimes. However, the incorporation of different STC schemes into land surface process models (LSMs) can afford large errors. Thus, to accurately simulate soil thermal regimes in permafrost regions, a suitable STC scheme in LSMs is important. Herein, we selected nine normalized STC schemes and evaluated their performance in simulating STC and soil temperatures with in situ measurements in permafrost regions on the Tibetan Plateau (TP). These schemes were divided into three categories and incorporated into the latest version of the Community Land Model (CLM5.0). The results showed that the category comprising minerals, soil organic matter, and gravel soil afforded better performance at most sites than the other categories. The Balland and Arp (BA2005), Chadburn (C2015), and Bao (B2016) schemes had better performances in their affiliated categories, respectively. The BA2005 scheme ranked the best among the selected schemes with an average root-mean-square error decreased of 56.2% and 15.0% in simulating STC and soil temperatures compared to the default scheme, respectively. Additionally, the different schemes yielded a maximum difference of 2.69 $W \cdot m^{-1} K^{-1}$ and 2.55 °C in simulating STC and soil temperature, respectively. Possible causes affecting the results were also investigated. The results indicated that soil moisture is a determinant: slight changes in soil moisture may cause large changes in thermal processes. However, the CLM5.0 yields large uncertainties of soil moisture. In addition, soil properties, atmospheric forcing data, and model structures also yielded errors in the simulated results. Note that no single STC scheme can be applied to all regions with satisfactory results. Therefore, multiple schemes need to be employed depending on their suitability in different regions. And more studies should focus on the accuracy of the hydraulic processes, especially soil hydraulic conductivity, unfrozen water, and snow processes.

1. Introduction

More than a quarter of the land area of the Northern Hemisphere is occupied by permafrost (Gruber, 2012). The Tibetan Plateau (TP) is underlain by the highest and most extensive permafrost region at mid-latitude (Qiu, 2008; Zhang et al., 2019; Zou et al., 2017). As an important component of the cryosphere, permafrost is a sensitive indicator of climate change (Ding et al., 2020; Yao et al., 2019). In recent decades, the permafrost on the TP has experienced dramatic warming and degradation, which has potentially triggered the release of greenhouse gases into the atmosphere (Cheng and Wu, 2007; Ding et al., 2020; Li et al., 2012; Mu et al., 2020; Ni et al., 2020). Consequently, realistically simulating permafrost thermal regimes in land surface process models (LSMs), which are generally used to understand regional characteristics and potential future changes, is essential. (Chadburn et al., 2015; Li et al., 2020; Zhang et al., 2019). Ensuring accurate physics processes in LSMs is the first step in simulating the thermal conditions of permafrost dynamics (Chadburn et al., 2015; He et al., 2020a; Li et al., 2020).

* Corresponding author.
E-mail address: liren@lzb.ac.cn (R. Li).

https://doi.org/10.1016/j.geoderma.2021.115330
Received 19 February 2021; Received in revised form 12 May 2021; Accepted 29 June 2021
Available online 15 July 2021

As an important thermal parameter in LSMs, soil thermal conductivity (STC) significantly influences the soil heat flux and vertical distribution of the soil temperature (Dai et al., 2019a; Farouki, 1981; He et al., 2020a). However, large-scale measured STC is difficult and impractical to obtain, especially in permafrost regions over the TP (Du et al., 2020; Li et al., 2019). In contrast, the parameterization of STC schemes can provide an efficient tool for understanding STC variations (Balland and Arp, 2005; Farouki, 1981; He et al., 2021; Peters-Lidard et al., 1998). Many theoretical and empirical STC schemes have been proposed based on soil properties, soil moisture, and porosity (de Vries, 1963; Farouki, 1981; Johansen, 1975; Kersten, 1949; McCumber and Pielke, 1981). Johansen (1975) first proposed the normalized scheme for estimating STC, which was calculated by interpolating between the dry and saturated soil thermal conductivities depending on the soil moisture content (He et al., 2020b). Based on the Johansen scheme, many derivative STC schemes have been proposed for different study areas and soil types, such as mineral (Bao et al., 2016; Farouki, 1981; He et al., 2017; Lu et al., 2007; Yang and Koike, 2005), organic matter (Balland and Arp, 2005; Chadburn et al., 2015; Chen et al., 2012; Lawrence and Slater, 2008), and considering gravel (Balland and Arp, 2005; Pan et al., 2015; Yi et al., 2018). Numerous studies have used in situ measurements or laboratory observations to determine the most suitable scheme (Chadburn et al., 2015; Du et al., 2020; Farouki, 1981; He et al., 2021, 2020a). Previous studies have shown that the different STC schemes afford soil temperature differences of 1–3 °C (Dai et al., 2019a; Peters-Lidard et al., 1998; Zhang et al., 2012). When these schemes are coupled with a model to simulate soil thermal regimes, the simulated errors will skew the understanding of the permafrost thermal regimes. Therefore, a suitable STC scheme needs to be selected for LSMs to accurately simulate permafrost thermal properties.

Recently, some related studies have been conducted in seasonally frozen ground regions (Dai et al., 2019a; He et al., 2020a; Peters-Lidard et al., 1998; Yi et al., 2018; Zhang et al., 2012). However, due to the scarcity of observation data, few studies have been conducted in permafrost regions where freeze–thaw frequent cycles occur. Furthermore, the performances and differences in various STC simulations for different STC schemes incorporated into LSMs remain unclear. Therefore, we conducted some related analyses in permafrost regions on the TP using the latest version of the Community Land Model (CLM5.0). Notably, many major components and processes have been updated in CLM5.0 (Lawrence et al., 2019). Studies compared the performance between CLM5.0 and CLM4.5 and suggested that CLM5.0 outperformed CLM4.5 concerning soil thermal properties and key parameters on the TP (Deng et al., 2020; Luo et al., 2020). In this study, we selected nine STC schemes to incorporate into CLM5.0 and collected data at six sites to assess the CLM5.0′s performance in simulating STC and soil temperatures in permafrost regions on the TP. Then, the differences and uncertainty factors resulting from different STC schemes in CLM5.0 were investigated and discussed. Finally, we recommend a suitable STC scheme for use in LSMs in permafrost regions and summarized possible efforts to obtain more accurate results in the future.

2. Materials and methods

2.1. Materials

2.1.1. In situ sites and measurements

Six sites in permafrost regions on the TP were selected to evaluate the performance of nine STC schemes incorporated into CLM5.0. The six sites extend from near the north limit (Xidatan, i.e., QT09) to the south limit of permafrost (Liangdaohe, i.e., CN04), and Tanggula (QT04) is the highest field site of permafrost on the TP (Sun et al., 2019; Yang et al., 2020). Additionally, these sites constitute different land cover types, representing the main vegetation types for permafrost regions over the TP (Hu et al., 2019; Wang et al., 2016; Yue et al., 2017). Therefore, the six selected sites appropriately reflect the permafrost characteristics over the TP (Fig. 1). Detailed information about the six sites is shown in Table 1. Due to harsh weather conditions and animal disturbances in permafrost regions on the TP, data were missing at these sites, especially during the frozen period. And the atmospheric forcing data for the QT03 site were derived from the article by Li et al (2020). Therefore, we collected high-quality data at these sites with the same period as the QT03 site. Soil temperature and moisture were used to analyze the performance of the simulated soil temperature and the influencing factors. The 109 and 105 T temperature probes (Campbell Scientific, Inc., USA) with an accuracy of 0.1 °C were employed to measure soil temperature, and the Stevens Hydro Soil Sensor (Stevens Water Monitoring System, Inc., USA) with an accuracy of ± 3% was employed to measure the soil moisture of the activity layer thickness from 2 to 320 cm below the surface. Probes were installed at 10–20 cm intervals in shallow layers and 20–80 cm intervals with increasing depth.

Due to the lack of observed STC data, only the topsoil STC data were collected, and they were ascertained through the soil heat flux and temperature gradient between 5 and 10 cm soil depths. This method can adequately account for variation characteristics in the topsoil STC (Farouki, 1986; Li et al., 2019). Soil heat fluxes at 5 and 10 cm below the surface were recorded using HFP01SC (Campbell Scientific, Inc., USA) with an accuracy of ± 3%. All instruments sampled the soils for 5 or 10 min, and data were averaged once over 30-min or 1-h using a CR1000 datalogger (Campbell Scientific Inc., USA) (http://new.crs.ac.cn/). The response time of the instruments was short (about 1–5 min), and the monitored data varied with time. Therefore, soil heat fluxes can be considered as instantaneous, and non-conductive heat transfer very small and they can be neglected (Li et al., 2019; Ren et al., 1999). Moreover, STC can be determined using a one-dimensional heat transfer equation as follows:

$$\lambda = -\frac{(G_i + G_j)/2}{\Delta T_s/\Delta z} \quad (1)$$

where λ (W m^{-1} K^{-1}) is soil thermal conductivity, G_i and G_j (W m^{-2}) are soil heat fluxes at i and j soil layers, respectively. ΔT_s (K) and Δz (m) is the soil temperature difference and thickness between two flow plates, respectively.

2.1.2. Atmospheric forcing data

The observed atmospheric forcing data, including the near-surface air temperature, wind speed, pressure, precipitation rate, specific humidity, downward shortwave radiation, and downward longwave radiation, with 30-min or 1-h temporal resolutions at the CN04, QT04, QT03, and QT09 sites were used to drive offline simulation in CLM5.0. The data at the QT12 and QT13 sites were extracted from the nearest neighboring grid of the China Meteorological Forcing Dataset (CMFD). This dataset was composed using remote sensing products, reanalysis datasets, and in situ site data, with a 3-h temporal resolution and 0.1° × 0.1° spatial resolution. The CMFD atmospheric forcing data accuracy has been acknowledged and has been widely used in simulations in various studies in China (Deng et al., 2020; Yang et al., 2018). This dataset is available online (https://data.tpdc.ac.cn/zh-hans/), and a detailed description of CMFD is present in He et al. (2020c).

2.2. Methods

2.2.1. Description of CLM5.0

The CLM is the land component of the Community Earth System Model (CESM, http://www.cesm.ucar.edu/models/cesm2/) and is used in regional and global modeling systems (Lawrence et al., 2019). CLM5.0 is the latest version of CLM and is an upgraded version of CLM4.5. Compared to CLM4.5, CLM5.0 incorporates many new and updated processes and parameterizations, including snow density, plant hydraulics, hydraulic redistribution, river model, and carbon and nitrogen cycling. Furthermore, CLM5.0 comprises higher numbers (especially within the top 3 m) and depths of soil layer than CLM4.5,

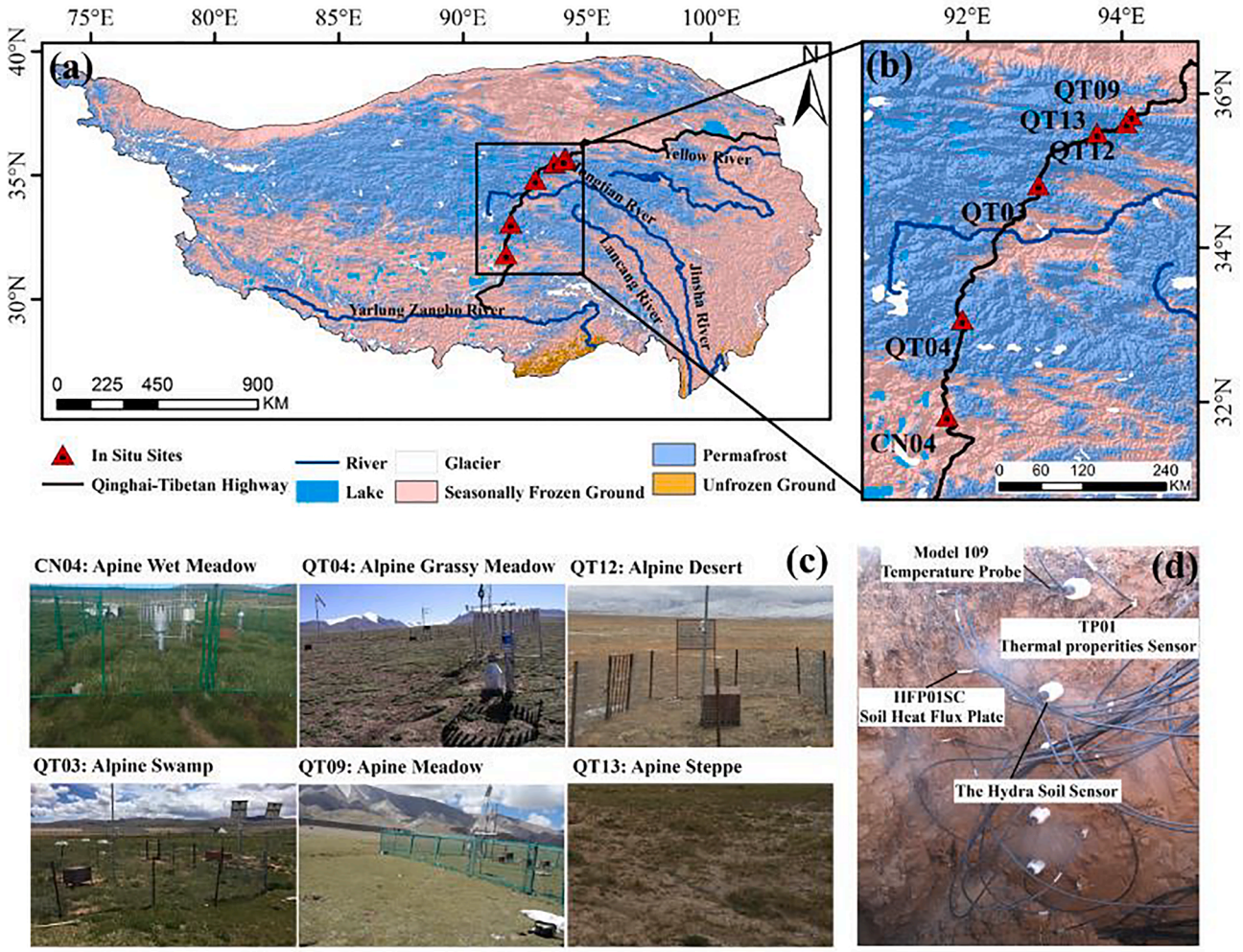

Fig. 1. Location of the monitoring sites on the Tibetan Plateau (TP). (a) The frozen-ground map of the TP was derived from Zou et al. (2017); (b) the location of the monitoring sites; (c) the different land cover types of the six sites; and (d) the monitoring instrument installation to observe the soil hydro thermal regimes at different depths.

Table 1
Information of in situ sites in permafrost regions on the TP.

Site number	Site name	Longitude (°E)	Latitude (°N)	Altitude (m)	Land cover type	Coverage (%)	Temporal coverage of data
CN04	Liangdaohe	91.74	31.82	4808	Alpine wet meadow	92.4	2017/01/01–2017/12/31
QT03	Beiluhe*	92.92	34.82	4656	Alpine swamp	81.7	2009/08/20–2009/08/19
QT04	Tanggula	91.93	33.07	5100	Alpine grassy meadow	51.3	2006/08/20–2007/08/19
QT09	Xidatan	94.13	35.72	4538	Alpine meadow	85.0	2013/08/20–2014/08/19
QT12	Kunlun Pass	94.06	35.62	4746	Alpine desert	12.3	2016/08/20–2017/08/19
QT13	Tedaqiao	93.68	35.49	4563	Alpine steppe	23.3	2016/08/20–2017/08/19

*The atmospheric forcing data at the QT03 derived from Li et al. (2020)

improving the simulation accuracy of the soil's hydrothermal regimes, especially in permafrost regions (Lawrence et al., 2019; Melton et al., 2019). The biggest difference between CLM4.5 and CLM5.0 is the soil evaporation parameterization, which was replaced by a dry surface layer-based soil resistance parameterization in CLM5.0 (Swenson and Lawrence, 2014). Subsequently, the subhumid and semiarid regions on the TP were found to contain more soil moisture than that previously determined (Deng et al., 2020). The STC parameterization in CLM4.5 was retained by CLM5.0 and is based on the Farouki scheme (Farouki, 1981) with the organic matter effect (Lawrence and Slater, 2008). A full technical description of CLM5.0 is available online (http://www.cesm.ucar.edu/models/cesm2/land/CLM50_Tech_Note.pdf). For more details on CLM5.0′s improvements, please see Lawrence et al. (2019). Overall, recent studies have confirmed that CLM5.0 simulated soil temperature on the TP better than CLM4.5 (Deng et al., 2020; Luo et al., 2020).

2.2.2. Model setup

Herein, we only ran single-point offline experiments and selected the Satellite Phenology Model (CLMSP). A 30-year spin-up simulation was conducted to reach an equilibrium of the hydrothermal regime, and the values after the initialization equilibrium for CLM5.0 were used. Although the gravel content is considered in some STC schemes, it was not incorporated into CLM5.0. Therefore, the fraction of gravel was added to CLM5.0 in this study. The observed surface data, including percent of sand, clay, and soil organic matter (SOM), vegetation height,

and vegetation proportion, were used to replace default values at each site. To address the lack of observed SOM at the QT12 and QT13 sites and the gravel data at the QT13 site, we derived these values from the China soil datasets (Shangguan et al., 2013).

2.2.3. Experimental designs

To determine the effects of the STC scheme on soil thermal properties, nine normalized STC schemes were incorporated into CLM5.0. These nine schemes were divided into three categories: (a) mineral soils category (particle diameter $\leq$ 2 mm); (b) mineral and SOM soils category; and (c) mineral, SOM, and gravel soils category (particle diameter $>$ 2 mm). Table 2 presents a summary of the nine STC schemes. Among the nine schemes, although SOM was considered by Côté and Konrad (2005) (CK2005) scheme, it was only for pure peat. Thus, in this study, we classified the CK2005 scheme into the mineral category. The scheme proposed by Lawrence and Slater (2008) (LS2008) is the default STC scheme in CLM5.0, and the other schemes are the Johansen (1975) (J1975) scheme and derivative schemes. All STC schemes have been validated by numerous experiments or in situ measurements and have been incorporated into different LSMs, such as the Joint UK Land Environment Simulator (JULES), the dynamic organic soil version of the Terrestrial Ecosystem Model (DOS-TEM), the Common Land Model (CoLM), and CLM (He et al., 2021, 2020a, 2017; Luo et al., 2017). Due to the lack of in situ measurements, the content of quartz is commonly considered to be equal to half of the sand content (Du et al., 2020; He et al., 2021).

Additionally, surface roughness is the main cause of heat flux variations under large amounts of heat in the ground (Peters-Lidard et al., 1998). Yang et al. (2008) proposed a scheme to determine the thermal roughness length (z_{oh}), and this scheme has been widely used in models (Li et al., 2020; Wang and Ma, 2018; Wu et al., 2018). We incorporated the scheme into CLM5.0 to improve simulation accuracy. This scheme is defined as

$$z_{oh} = \left(\frac{70v}{\mu_*}\right) \times exp\left(-\beta\mu_*{}^{0.5}|T_*|^{0.25}\right) \quad (2)$$

$$v = v_0\left(\frac{p_0}{p}\right)\left(\frac{T}{T_0}\right)^{1.754} \quad (3)$$

Table 2
The information of selected STC schemes.

Reference	Abbreviation	Expressions
Mineral soils category		
Johansen, 1975	J1975	$\lambda = K_e(\lambda_{sat} - \lambda_{dry}) + \lambda_{dry}$, $K_e = \begin{cases} 0.7logS_r + 1.0, 0.05 < S_r < 0.1 unfrozensoils \\ logS_r + 1.0, S_r > 0.1 unfrozensoils \\ S_r, frozensoils \end{cases}$, $\lambda_{sat} = \begin{cases} \lambda_w{}^n\lambda_s{}^{1-n}, unfrozensoils \\ \lambda_w{}^{\theta_l}\lambda_s{}^{1-n}\lambda_{ice}{}^{n-\theta_l}, frozensoil \end{cases}$, $\lambda_s = \lambda_q{}^{\phi_q}\cdot\lambda_o{}^{1-\phi_q}$, $\lambda_{dry} = \frac{0.135\rho_b + 64.7}{\rho_s - 0.947\rho_b}$
Farouki, 1981	F1981	$\lambda = \begin{cases} K_e(\lambda_{sat} - \lambda_{dry}) + \lambda_{dry}, S_r > 10^{-7} \\ \lambda_{dry}, S_r > 10^{-7} \end{cases}$, $K_e = \begin{cases} logS_r + 1.0, T \geq T_f \\ S_r, T < T_f \end{cases}$, $\lambda_{sat} = \begin{cases} \lambda_w{}^n\lambda_s{}^{1-n}, unfrozensoils \\ \frac{\theta_l \cdot n}{\lambda_w\theta_l + \theta_{ice}}\lambda_s{}^{1-n}\lambda_{ice}{}^{n\left(1-\frac{\theta_l \cdot}{\theta_l + \theta_{ice}}\right)}, frozensoil \end{cases}$, $\lambda_s = \frac{8.8(\phi_{sand}) + 2.92(\phi_{clay})}{(\phi_{sand}) + (\phi_{clay})}$, λ_{dry} is same as J1975
Côté and Konrad, 2005	CK2005	λ, and λ_{sat} are same as J1975, $K_e = \frac{kS_r}{1 + (k-1)S_r}$, $\lambda_{dry} = \chi 10^{-n\eta}$
Luo et al., 2009	L2009	$\lambda = \begin{cases} K_e(\lambda_{sat} - \lambda_{dry}) + \lambda_{dry}, S_r > 10^{-5} \\ \lambda_{dry}, S_r > 10^{-5} \end{cases}$, λ_{sat} is same as J1975K_e and λ_{dry} are same as CK2005,
Bao et al., 2016	B2016	$\lambda = K_e(\lambda_{sat} - \lambda_{dry}) + \lambda_{dry} + 2.2\theta_{ice}$, $K_e = exp\left[0.36\left(1 - \frac{1}{S_r}\right)\right]$, $\lambda_{sat} = \lambda_w{}^n\lambda_s{}^{1-n}$, λ_s and λ_{dry} are same as J1975
Mineral and soil organic matter (SOM) soils category		
Lawrence and Slater, 2008	LS2008	λ, K_e, and λ_{sat} are same as F1981, $\lambda_s = (1 - \phi_{om})\left[\frac{8.8(\phi_{sand}) + 2.92(\phi_{clay})}{(\phi_{sand}) + (\phi_{clay})}\right] + \phi_{om}\cdot\lambda_{om}$, $\lambda_{dry} = (1 - \phi_{om})\left(\frac{0.135\rho_b + 64.7}{\rho_s - 0.947\rho_b}\right) + \phi_{om}\lambda_{om\_dry}$
Chadburn et al., 2015	C2015	λ, and K_e are same as J1975, $\lambda_{sat} = \lambda_{sat,0}\frac{\frac{\theta_l \cdot n}{\lambda_w\theta_l + \theta_{ice}}\lambda_{ice}{}^{n\left(\frac{\theta_{ice}}{\theta_l + \theta_{ice}}\right)}}{\lambda_w{}^n}$, $\lambda_{sat,0} = \begin{cases} 0.5, \lambda_{dry} < 0.06 \\ \frac{1 - 0.0134ln(\lambda_{dry})}{-0.745 - ln(\lambda_{dry})}, 0.06 < \lambda_{dry} < 0.3 \\ 2.2, \lambda_{dry} > 0.3 \end{cases}$, $\lambda_{dry} = \lambda_{min}{}^{1-\phi_{om}}\cdot\lambda_{om\_dry}{}^{\phi_{om}}$
Mineral, SOM, and gravel soils category		
Balland and Arp, 2005	BA2005	$\lambda$and λ_{sat} are same as J1975, $K_e = \begin{cases} S_r{}^{0.5(1+\phi_{om}-\alpha\phi_{sand}-\nu\phi_g)}\left\{\left[\frac{1}{1+e^{-\beta S_r}}\right]^3 - \left(\frac{1-S_r}{2}\right)^3\right\}^{1-\phi_{om}}, unfrozensoils \\ S_r{}^{1+\phi_{om}}, frozensoils \end{cases}$, $\lambda_s = \lambda_{om}{}^{\phi_{om}}\lambda_q{}^{\phi_q}\cdot\lambda_o{}^{(1-\phi_q-\phi_{om})}$, $\lambda_{dry} = \frac{(0.053\lambda_s - \lambda_{air})\rho_b + \lambda_{air}\rho_s}{\rho_s - 0.947\rho_b}$
Dai et al., 2019a	D2019	$\lambda$and K_e are same as BA2005, $\lambda_{sat} = \lambda_s{}^{\phi_{min}}\lambda_{om}{}^{\phi_{om}}\lambda_g{}^{\phi_g}\lambda_{w/i}{}^n$, $\lambda_s = \lambda_q{}^{\phi_q}\cdot\lambda_o{}^{(1-\phi_q)}$, $\lambda_{w/i} = \begin{cases} 0.57, unfrozensoil \\ 2.29, frozensoil \end{cases}$, $\lambda_{dry} = \phi_{min}\lambda_{min} + \phi_{om}\lambda_{om\_dry} + \phi_g\lambda_g$, $\lambda_{min} = \frac{0.135\rho_b + 64.7}{\rho_s - 0.947\rho_b}$, $\lambda_g = 0.039n^{-2.2}$

*λ: Soil thermal conductivity (W m^{-1} K^{-1}); K_e: Kersten number; λ_{sat}: Saturated thermal conductivity (W m^{-1} K^{-1}); λ_{dry}: Thermal conductivity of dry soil (W m^{-1} K^{-1}); λ_q: Thermal conductivity of quartz (7.7 W m^{-1} K^{-1}); ϕ_{sand}: Volumetric fraction of sand (%); ϕ_{clay}: Volumetric fraction of clay (%); ϕ_q: Volumetric fraction of quartz ($\phi_q = 0.5\phi_{sand}$, %); ϕ_{om}: Volumetric fraction of organic matter (%); ϕ_g: Volumetric fraction of gravel (%); λ_w: Thermal conductivity of water (0.57 W m^{-1} K^{-1}); λ_{ice}: Thermal conductivity of ice (2.29 W m^{-1} K^{-1}); λ_o: Thermal conductivity of other minerals (λ_o = 2.0 W m^{-1} K^{-1} for $\phi_q > 20$, and 3.0 W m^{-1} K^{-1} for $\phi_q \leq 20$); λ_{air}: Thermal conductivity of air (0.025 W m^{-1} K^{-1}); λ_s: Thermal conductivity of soil solids (W m^{-1} K^{-1}); λ_g: Thermal conductivity of gravel (W m^{-1} K^{-1}); ρ_b: Bulk density (kg m^{-3}); ρ_s: Particle density (2700 kg m^{-3}); θ: Volumetric total water content (m^3 m^{-3}); θ_l: Volumetric liquid water content (m^3 m^{-3}); θ_{ice}: Volumetric ice content (m^3 m^{-3}); S_r: Degree of saturation; n: Soil porosity; λ_{om_dry}: Thermal conductivity of organic matter (0.25 W m^{-1} K^{-1}); λ_{min}: Thermal conductivity of mineral (W m^{-1} K^{-1}); χ, k, and η: Parameters of the CK2005 and L2009 schemes, the detail can be found in Table A.1 and Table A.2 in the supplementary file.

$$T_* = -H/(\rho_a C_P \mu_*) \quad (4)$$

where $\beta = 7.2 m^{-\frac{1}{2}} s^{\frac{1}{2}} K^{-\frac{1}{4}}$; $\nu(m^2 s^{-1})$ is the air kinematic viscosity; $\mu_*(ms^{-1})$ is the friction velocity; $T_*(K)$ is the temperature scale; $H(Wm^2)$ is the sensible heat flux; $\rho_a(kgm^{-3})$ is the air density; $T(K)$ is surface air temperature; $p_0 = 1.013 \times 10^5\ Pa$; and p is the surface pressure; $\nu_0 = 1.328 \times 10^{-5} m^2 s^{-1}$; $T_0 = 273.15K$; and $C_P = 1004 Jkg^{-1} K^{-1}$.

2.3. Statistical metrics

To reduce the uncertainty of in situ measurements, we analyzed the daily averaged value of the simulations and observations, and divided the study into two periods (frozen and thawed) depending on the soil temperature. To avoid the influence of random fluctuations on soil temperature, the freeze and thaw onsets were determined based on the average of the daily soil temperatures taken for five consecutive days; they were below and above 0 °C, respectively, and varied depending on the soil layer (Guo and Wang, 2014). In this study, four statistical metrics, the correlation coefficient (*R*), mean bias error (*MBE*), mean absolute error (*MAE*), and root-mean-square error (*RMSE*) were employed to evaluate the performances of the nine STC schemes. These metrics are defined as

$$R = \frac{\sum_{i=1}^{N}(M_i - \overline{M})(O_i - \overline{O})}{\sqrt{\sum_{i=1}^{N}(M_i - \overline{M})^2} \cdot \sqrt{\sum_{i=1}^{N}(O_i - \overline{O})^2}} \quad (5)$$

$$MBE = \frac{1}{N}\sum_{i=1}^{N}(M_i - O_i) \quad (6)$$

$$MAE = \frac{1}{N}\sum_{i=1}^{N}|(M_i - O_i)| \quad (7)$$

$$RMSE = \sqrt{\frac{1}{N}\left(\sum_{i=1}^{N}(M_i - O_i)^2\right)} \quad (8)$$

where N is the time series length, $M_i(i = 1, 2, \cdots N)$ is the simulated value, O_i is the observed value, and $\overline{M}$ and $\overline{O}$ represent the average values of simulated and observed, respectively.

To comprehensively evaluate the performance of the nine STC schemes, the following ranking model was used (Brunke et al., 2003; Wang and Zeng, 2012):

$$Rank = \frac{1}{n}\sum_{i=1}^{n} Score_i \quad (9)$$

where n is the number of metrics, and $Score_i$ is based on different STC schemes order of performance on the *ith* metric (i.e., the best is 1 and the worst is 9). Ultimately, the nine STC schemes were ranked from 1 (best) to 9 (worst) based on the average score of all metrics. This method can convert all metrics to dimensionless values, which is similar to the normalization method. Note that the *MBE* metric exhibits both positive and negative values, resulting in the underestimation of *MBE* results. Therefore, the *MBE* metric was not considered in the ranking. However, compared to the observation value, the simulated value can be an overestimation (positive value) or underestimation (negative value).

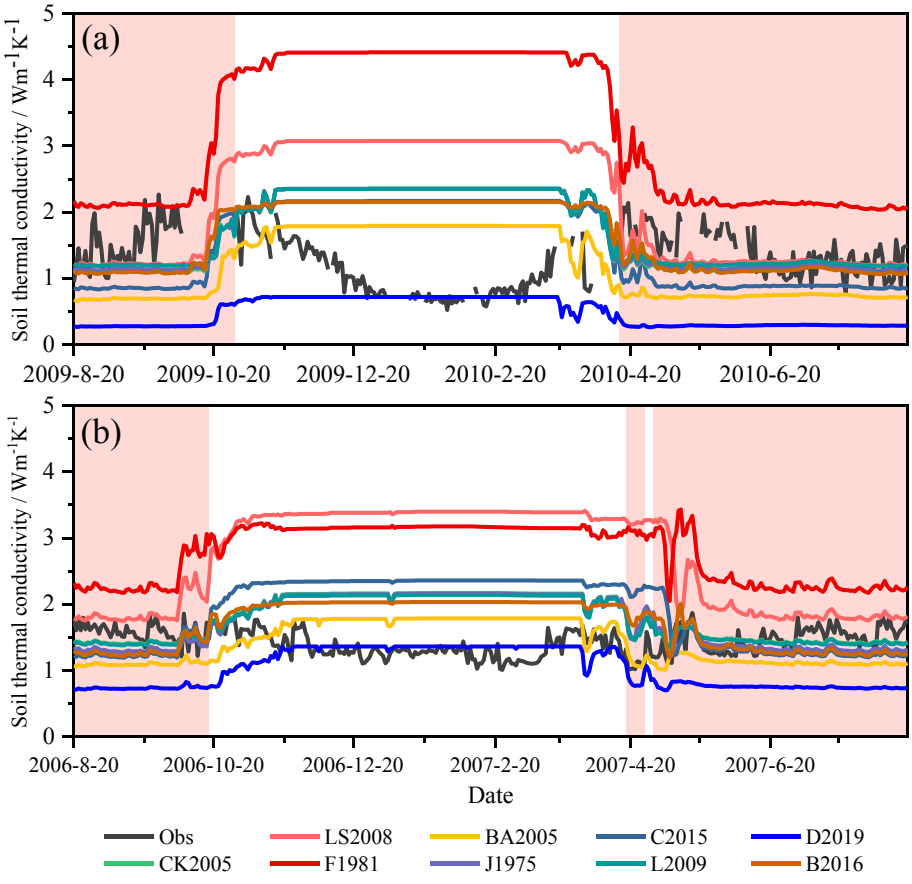

Fig. 2. Variations in the observed soil thermal conductivity (STC) (black line) and STC simulated by CLM5.0 with nine STC schemes at 5 cm soil depth at the QT03 (a) and QT04 (b) sites. The shaded and white areas represent the thawed and the frozen periods, respectively.

3. Results

3.1. Evaluations of STC simulated by different STC schemes

Due to the lack of in situ measurements, only STC data at 5 cm soil depth from the QT03 and QT04 sites were used to evaluate the performances of the different schemes in STC in permafrost regions on the TP. Fig. 2 shows the variation patterns in the simulated STC for the nine STC schemes incorporated into CLM5.0 against in situ measurements at 5 cm depth at the QT03 and QT04 sites. Table 3 presents the error statistics of the nine STC schemes at the two sites. As demonstrated, the STC values simulated by the different schemes are similar and they are close to the measured values at the two sites during the melting period. However, other than the D2019 scheme, the STC values of the frozen period were significantly overestimated by STC schemes, especially the F1981 and LS2008 schemes. Note that, the measured STC values during the frozen period were lower than those of the thawed period with ratios of 0.78 and 0.91 at the QT03 and QT04 sites, respectively. However, contradictory trends were simulated by the nine STC schemes (Fig. 2 and Table 4).

To evaluate the performance of the nine STC schemes incorporated into CLM5.0 in determining STC, we calculated the rank score according to Eq. (9) for each STC scheme at the two sites, as displayed in Fig. 3. The BA2005 and D2019 schemes outperform the other schemes during the frozen period at the two sites, but they afford poor performances during the thawed period (Fig. 3b and c). The LS2008 and CK2005 schemes are superior to the other schemes during the thawed period at the QT03 and QT04 sites, respectively. The BA2005, C2015, and L2009 schemes have better performances in their affiliated categories, respectively. Overall, during the entire study period, the BA2005 scheme ranked the best among the nine STC schemes in simulating STC at the two sites with the *RMSE* decreases of 56.2.0% compared to the default scheme (i.e., LS2008), followed by the L2009 and B2016 schemes. The F1981 and LS2008 schemes yield unsatisfactory results at the two sites (Fig. 3a).

3.2. Evaluations of soil temperature simulated by different STC schemes

The soil temperatures of different soil layers were directly determined using the STC; thus, the nine STC schemes' performances in simulating soil temperatures were also evaluated. Fig. 4 illustrates the changes in the simulated soil temperatures and in situ measurements at different soil depths at six sites in permafrost regions on the TP. All STC schemes incorporated into CLM5.0 capture the temporal pattern of the soil temperature at the six sites. The differences among the simulated soil temperatures obtained using different STC schemes are small in the shallow layers, but they increase with depth. The error statistics of the nine STC schemes are displayed in Fig. 5. The soil temperatures for the thawed period are overestimated and that for the frozen period are underestimated, except for the QT13 site. Note that the simulated errors are larger at the QT13 and the QT09 sites (Fig. 5b and d).

Similarly, we also calculated the rank score of the nine STC schemes regarding the simulated soil temperatures in each soil layer at the six sites (Fig. 6). The results show that mineral, SOM, and gravel soils category performs better than the other categories at most sites. Moreover, the BA2005, C2015, and B2016 schemes exhibit superiority regarding soil temperature in their affiliated categories. Particularly, the BA2005 scheme ranks the best among these schemes at most sites, with an average *RMSE* reduction of 15.0% (maximum 44.8%) compared to the default scheme (i.e., LS2008) (Fig. 5c). However, during the thawed period, the BA2005 scheme afford unsatisfactory results at the QT04 and QT13 sites. Additionally, STC schemes performances exhibit considerable discrepancies under different land cover types. The BA2005 scheme displays the best performance for the alpine wet meadow, alpine meadow, and alpine desert. Furthermore, the C2015, CK2005, and B2016 schemes yield more accurate soil temperatures for the alpine swamp than those for other land covers. The LS2008 scheme provides the best performance for the alpine steppe. Similar to the STC results, the F1981 scheme affords worse accuracy for soil temperatures at most sites, but surprisingly, it displayed the best performance for the alpine grassy meadow and the alpine steppe, except for soil depths below 80 cm (Fig. 6a).

3.3. Comparison of relative differences among the nine STC schemes

To further ascertain the errors in the nine STC schemes incorporated into CLM5.0, we analyzed the relative differences among the nine STC schemes concerning the simulated STC and soil temperatures. Figs. 7 and 8 present the relative differences among the nine STC schemes

Table 3
Error statistics in the soil thermal conductivity (STC) simulated by CLM5.0 with the nine schemes at the QT03 and QT04 sites.

Site	State	Metrics	BA 2005	D2019	LS 2008	C2015	J1975	F1981	CK 2005	L2009	B2016
QT03	Study period	*RMSE*	**0.80**	0.99	1.36	0.9	0.92	2.29	0.93	0.91	0.82
		R	**−0.47****	−0.44**	−0.40**	−0.41**	−0.46**	−0.39**	−0.45**	−0.46**	−0.39**
		MAE	0.72	0.83	1.03	0.77	0.73	1.87	0.73	0.71	**0.66**
		MBE	**−0.12**	−0.82	0.77	0.15	0.37	1.87	0.36	0.40	0.29
	Frozen period	*RMSE*	0.81	**0.63**	1.97	1.12	1.28	3.27	1.28	1.28	1.11
		R	−0.54**	−0.40**	**−0.56****	−0.45**	−0.55**	−0.49**	−0.55**	**−0.56****	−0.42**
		MAE	0.73	**0.45**	1.91	1.02	1.17	3.23	1.17	1.17	1.01
		MBE	0.59	**−0.43**	1.91	1.00	1.15	3.23	1.15	1.15	1.01
	Thawed period	*RMSE*	0.80	1.21	**0.37**	0.65	0.44	0.78	0.46	0.41	0.46
		R	−0.23**	−0.30**	0.28**	0.21**	0.04	**0.37****	0.02	0.05	0.26**
		MAE	0.72	1.16	**0.29**	0.56	0.35	0.72	0.37	0.32	0.36
		MBE	−0.72	−1.16	**−0.19**	−0.56	−0.28	0.72	−0.31	−0.23	−0.32
QT04	Study period	*RMSE*	**0.44**	0.58	1.52	0.76	0.58	1.46	0.58	0.56	0.53
		R	−0.43**	−0.43**	**−0.46****	−0.44**	−0.43**	−0.37**	−0.42**	−0.41**	−0.40**
		MAE	**0.39**	0.48	1.26	0.65	0.48	1.36	0.46	0.45	0.46
		MBE	**−0.02**	−0.41	1.26	0.43	0.31	1.36	0.35	0.33	0.26
	Frozen period	*RMSE*	0.45	**0.31**	1.99	0.98	0.77	1.78	0.78	0.75	0.67
		R	−0.48**	−0.50**	−0.47**	−0.45**	**−0.55****	−0.35**	−0.51**	−0.50**	−0.46**
		MAE	0.40	**0.23**	1.97	0.95	0.72	1.77	0.72	0.70	0.63
		MBE	0.31	**−0.09**	1.97	0.95	0.71	1.77	0.72	0.69	0.63
	Thawed period	*RMSE*	0.43	0.77	0.74	0.41	0.27	1.00	**0.22**	**0.22**	0.32
		R	−0.05	−0.24**	**−0.49****	−0.48**	−0.25**	−0.21**	−0.17**	−0.14*	−0.27**
		MAE	0.39	0.75	0.51	0.33	0.24	0.92	**0.18**	**0.18**	0.27
		MBE	−0.38	−0.75	0.51	−0.14	−0.13	0.92	**−0.04**	−0.05	−0.14

*The bold values represent the best result for each error statistics among the nine soil thermal conductivity, $^{**}p < 0.01$, $^{*}p < 0.05$

Table 4
The ratio of the soil thermal conductivity between the frozen and the thawed period.

Site	Period/Ratio	Obs	BA2005	D2019	LS2008	C2015	J1975	F1981	CK2005	L2009	B2016
QT03	Frozen period	1.13	1.71	2.28	3.03	0.70	2.13	2.28	2.28	1.76	2.02
	Thawed period	1.44	0.72	0.29	1.26	0.88	1.16	2.16	1.13	1.22	1.12
	The ratio	0.78	2.38	7.98	2.42	0.79	1.84	1.05	2.02	1.45	1.80
QT04	Frozen period	1.37	1.68	1.28	3.34	2.32	2.08	3.13	2.09	2.06	2.00
	Thawed period	1.50	1.12	0.75	2.01	1.36	1.37	2.41	1.46	1.45	1.35
	The ratio	0.91	1.50	1.70	1.66	1.70	1.52	1.30	1.43	1.42	1.48

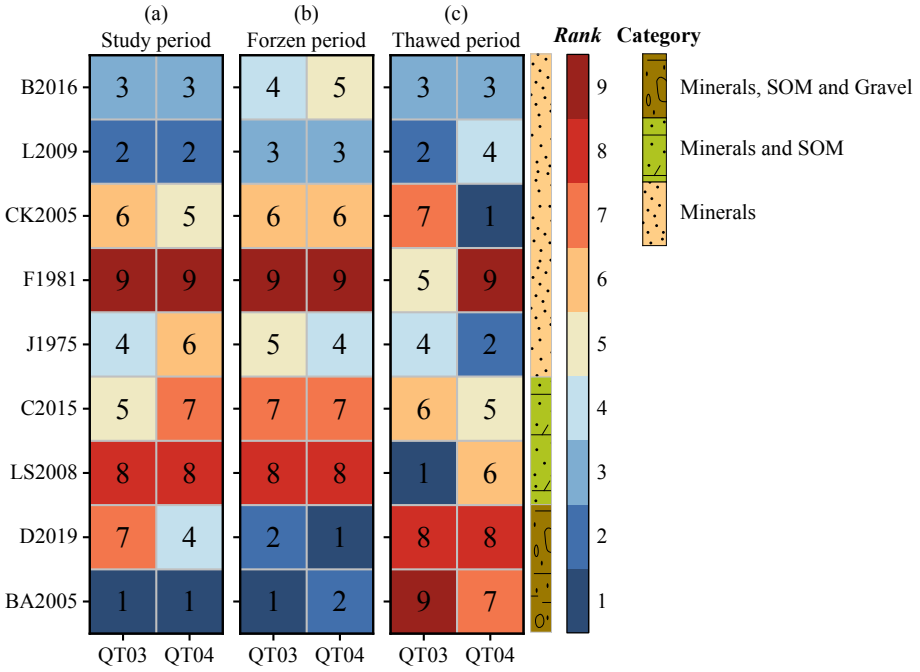

Fig. 3. Comprehensive rank scores for the simulated soil thermal conductivity (STC) based on correlation coefficient (R), root-mean-square (RMSE), and mean absolute error (MAE) at the QT03 and QT04 sites. (a) Study period, (b) frozen period, and (c) thawed period. Each scheme is ranked from 1 (best) to 9 (worst).

regarding the STC and soil temperature simulations, respectively. The differences in terms of STC simulations during the frozen period are greater than those during the thawed period, and the maximum difference is observed between the F1981 and D2019 schemes: 2.69 and 1.76 $W{\cdot}m^{-1}\,K^{-1}$ at the QT03 and QT04 sites, respectively. Similar results are obtained regarding soil temperatures (Fig. 8); the difference between the F1981 and D2019 schemes is 2.55 °C during the thawing period. Additionally, the differences in simulated soil temperatures increase with soil depth, and the maximum difference occurs at a soil depth of 80 cm (Fig. 8c, g, and k).

4. Discussion

4.1. Comparison with other similar analyses

In this study, we evaluated the performance of nine STC schemes incorporated into CLM5.0 in simulating STC in permafrost regions over the TP. Although some similar studies in other regions have been conducted, they generally compared the performances of different schemes directly by simulating the STC and did not incorporate them into models (Dai et al., 2019a; Peters-Lidard et al., 1998; Zhang et al., 2012). This approach can provide a direct method for evaluating STC scheme performances. However, many parameters of the schemes are based on observations (e.g., soil moisture, temperature, and porosity), which are parameterized in LSMs (Lawrence et al., 2019). Therefore, unsatisfactory results were obtained when the schemes were incorporated into LSMs (He et al., 2020a). Compared to other studies, we focused on the effects of different STC schemes incorporated into CLM5.0 on the simulated results. This facilitated an objective assessment of the STC scheme performances in LSMs and provided a reference for model improvements. Our results show that the different schemes well simulate STC during the thawed period but yield large errors during the frozen period (Fig. 2 and Table 3). Similar results have also been obtained for other regions (Du et al., 2020; Hu et al., 2017). The nine STC schemes were proposed based on soil samples across different to reflect the soil's spatial heterogeneity (Balland and Arp, 2005; Farouki, 1981; Luo et al., 2009). Therefore, the applicability of these schemes was also limited, further demonstrating the significance of this study. Moreover, our results illustrate that the BA2005 and D2019 schemes outperform the other schemes during the frozen period, whereas the L2009 and B2016 schemes yield better performances during the thawed period. These results are similar to those of other studies (Dai et al., 2019a; He et al., 2020a, 2021). Additionally, the BA2005 scheme affords the worst performance during the thawed period, but it ranks the best during the overall study period (Fig. 3). This is because STC is moderately underestimated during the frozen period and overestimated during the thawed period (Fig. 2 and Table 3), yielding better average results than those for the other schemes.

Generally, the STC of the frozen period was expected to be greater than that of the thawed period, and this phenomenon is commonly recognized because the thermal conductivity of ice (2.29 $W{\cdot}m^{-1}\,K^{-1}$) is four times that of water (0.57 $W{\cdot}m^{-1}\,K^{-1}$) (Domine et al., 2016; Du et al., 2020; Hinzman et al., 1991; Li et al., 2019). However, opposite characteristics were observed in this study (Fig. 2) and previous studies

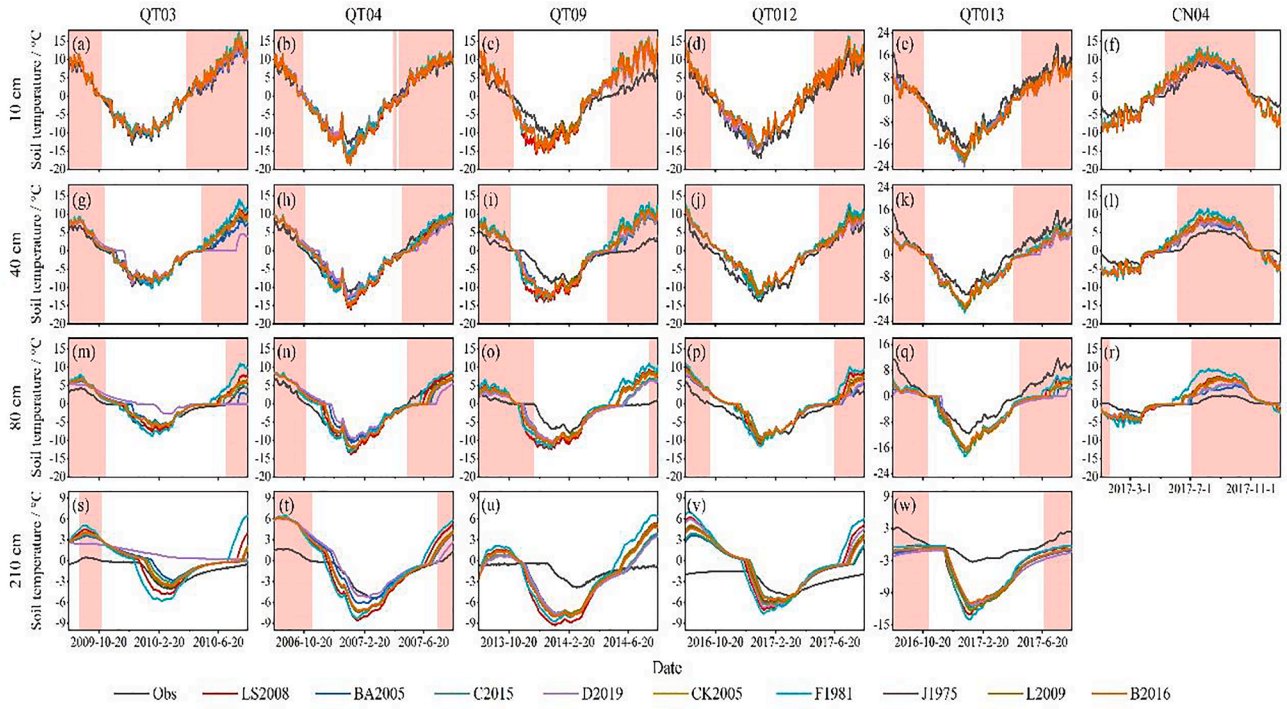

Fig. 4. Variations in the observed soil temperature and the simulated by CLM5.0 with the nine soil thermal conductivity schemes at different soil depths at the six sites. The shaded and white areas represent the thawed and frozen periods, respectively.

(Côté and Konrad, 2005; Du et al., 2020; Farouki, 1981; Li et al., 2019). Slusarchuk and Watson (1975) indicated that many small air bubbles and discontinuities in ice-rich permafrost soil were the main contributors to this. Recently, Li et al. (2019) have shown that STC was dependent on the initial freezing soil moisture content, and a similar trend was observed when the soil moisture content was less than the threshold (i.e., 0.195 $m^3 \cdot m^{-3}$ at the Tanggula on the TP). Subsequently, this conclusion was confirmed by Du et al. (2020) in other regions. In this study, the initial freezing soil moisture contents were 0.15 and 0.12 $m^3 \cdot m^{-3}$ at the QT03 and QT04 sites, respectively, which was consistent with the findings of Li et al. (2019).

Furthermore, we evaluated the effects of different STC schemes on soil temperature. Our results indicate that different STC schemes incorporated into CLM5.0 can result in maximum simulated errors of 2.55 °C in soil temperature (Fig. 8). This is consistent with the results of previous studies in other regions (Dai et al., 2019a; Peters-Lidard et al., 1998), further confirming that a suitable STC scheme coupled with LSMs is critical for obtaining accurate soil temperatures. Previous studies have suggested that the J1975, LS2009, and CS2015 schemes performed good surface ground temperature measurements in seasonally frozen ground regions (He et al., 2020a; Luo et al., 2009; Peters-Lidard et al., 1998). Our comparisons revealed that these STC schemes yielded good simulated results for soil temperatures, but the BA2005 scheme afforded the best performance with an average *RMSE* reduction of 15.0% compared to that of the default scheme (LS2008). A major reason for this is that the BA2005 scheme considers more soil components (i.e., mineral, SOM, gravel, and air in soils) than the other schemes, providing a more realistic representation of soil structure and applicability to a greater variety of soil types (Balland and Arp, 2005). Recently, Dai et al. (2019a) have evaluated the seven STC schemes incorporated into CoLM and suggested that the D2019 scheme was better than other schemes for simulating soil temperatures in the Nagqu and Arou sites on the TP. In our study, both the D2019 and BA2005 schemes yielded good-simulation results, but the BA2005 scheme is more suitable for most sites in permafrost regions on the TP (Figs. 3 and 6). The main difference between the two schemes is that the D2019 scheme added the gravel term to all parameters, whereas the BA2005 scheme only added gravel to the *Ke* number (Table 2). Gravel can increase porosity and thus reduce the thermal conductivity value in soil (Pan et al., 2015; Yi et al., 2018). Moreover, the D2019 scheme has not been validated by a large number of observations; thus, be careful when using it in other regions.

Additionally, our results showed that the F1981 and LS2008 schemes notably overestimate STC (Fig. 2 and Table 3), and they afforded larger errors in simulating soil temperatures than the other schemes at most sites (Figs. 5 and 6). Similar results have been also obtained by other studies (Dai et al., 2019a; Du et al., 2020; Hu et al., 2017). The F1981 scheme fails to consider the quartz contents, which causes the STC value of soil solids to be significantly overestimated (Hu et al., 2017). Additionally, the F1981 scheme oversimplifies the formula of the Kersten number (He et al., 2021). Organic matter and gravel in the soil can yield smaller STC values (Chen et al., 2012; He et al., 2020a; Lawrence and Slater, 2008), but they are not considered in the F1981 scheme. The only difference between the LS2008 and F1981 schemes is that SOM is incorporated into the LS2008. Therefore, the same deficiencies are present in the LS2008 scheme.

4.2. Possible causes for simulation errors in the schemes

4.2.1. The influence of soil moisture

The nine STC schemes selected herein are based on the concept of the J1975 scheme, which was calculated STC by interpolating between the dry and saturated conductivities depending on the soil water content (Johansen, 1975). Therefore, soil moisture is an essential factor, which has been widely recognized (Farouki, 1981; Du et al., 2020; He et al., 2020a; Li et al., 2019). As mentioned above, the soil ice and initial freezing soil moisture contents affects the STC values during the frozen period. However, this is not well reflected in CLM5.0. Unlike other regions, ice and unfrozen water coexist during the frozen period in permafrost regions (Hu et al., 2020; Li et al., 2019; Zhang et al., 2017). Although the unfrozen water parameter has been incorporated into CLM5.0, it still has a large error in permafrost regions on the TP (Niu and Yang, 2006; Hu et al., 2020). Moreover, soil ice content is an important

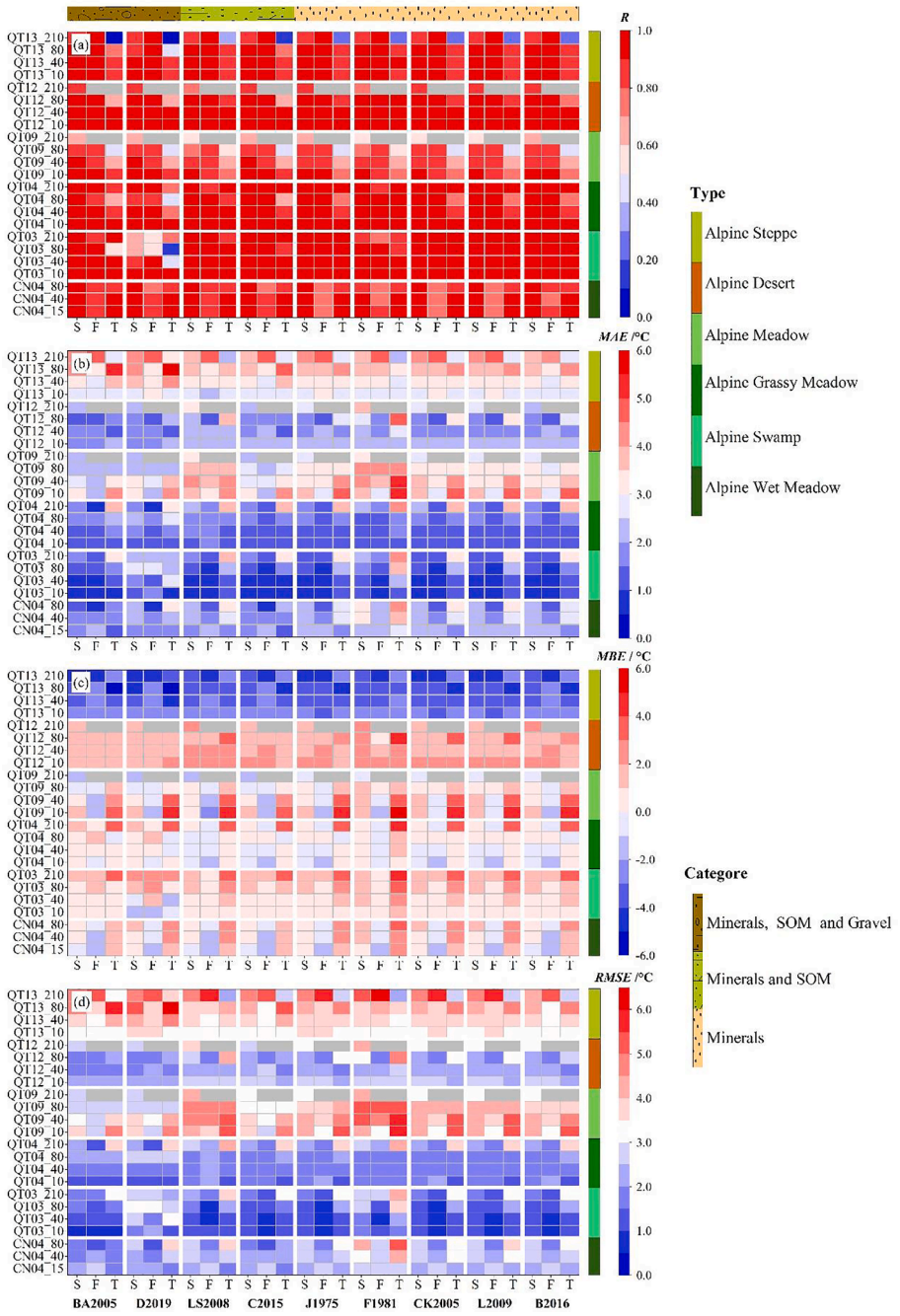

Fig. 5. The correlation coefficient (*R*) (a), mean absolute error (*MAE*) (b), mean bias error (*MBE*) (c), and root-mean-square error (*RMSE*) (d) of the nine soil thermal conductivity schemes regarding the soil temperatures at different soil depths at the six sites. S, F, and T on the x-axis represent the study, frozen, and thawed periods, respectively; the y-axis (unit: cm) represent the different soil depths at the six sites. Light gray areas represent missing observations.

part of the permafrost, but it is difficult to measure (Zhou et al., 2014). Hence, soil ice is calculated based on total water, liquid water, and unfrozen water in CLM5.0. Recent studies have indicated that the simulated soil moisture by CLM5.0 has a large uncertainty on the TP (Deng et al., 2020; Luo et al., 2020), resulting in large errors in the simulated STC during the frozen period. Furthermore, the differences in soil temperatures increase with the soil depth, and the maximum value occurs at a soil depth of 80 cm (Fig. 8c, g, and k); these differences were mainly related to the soil moisture. The simulated errors in the soil moisture increased with the depth in LSMs, and the largest fluctuations and errors occurred near a soil depth of 80 cm (Li et al., 2020; Yang et al., 2018). However, observing changes in soil moisture in deep layers is difficult for LSMs (Li et al., 2020). Similar phenomena have also been observed in reanalysis products of soil moisture (Qin et al., 2017; Yang et al., 2020).

To further investigate the relationship between STC schemes and soil moisture in CLM5.0, we compared the soil moisture derived from the default STC scheme (LS2008), the superior STC scheme (BA2005), and the in situ measurements. Due to data limitations, we only present the results for a soil depth of 10 cm, and also display the changes in precipitations (Fig. 9). The figure illustrates that the characteristics of changes in soil moisture are in good agreement with precipitation. Note that, soil moisture is underestimated at all sites, except for the QT13 site during the thawed period (Fig. 9e). This further explains the underestimation of the soil temperature at this site and the overestimation at other sites (Fig. 5b). Previous studies highlighted that the latent heat

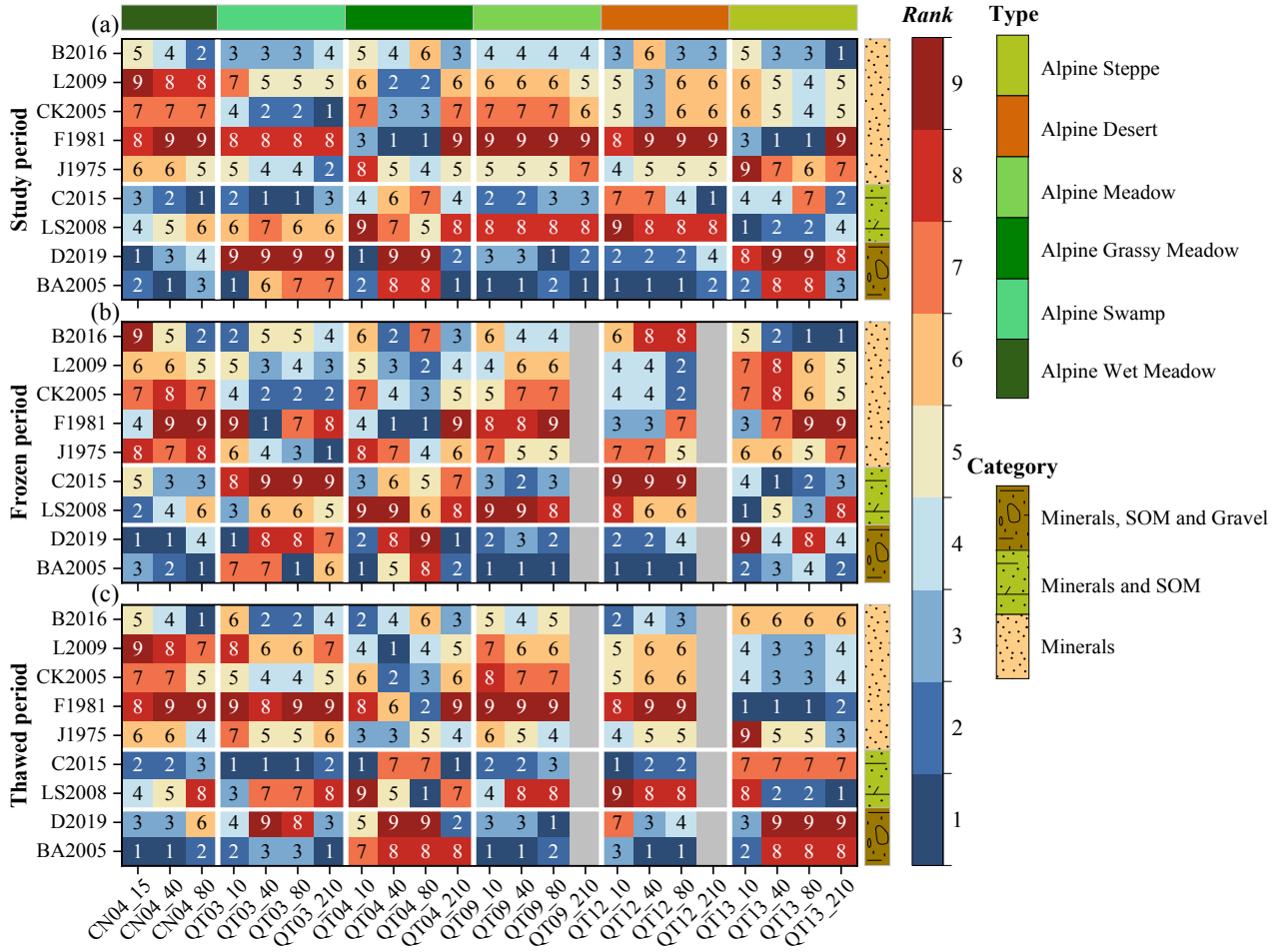

Fig. 6. Comprehensive rank scores for the simulated soil temperatures at the six sites. (a) Study period, (b) frozen period, and (c) thawed period. Each scheme is ranked from 1 (best) to 9 (worst) based on the correlation coefficient (*R*), root-mean-square error (*RMSE*), and mean absolute error (*MAE*) metrics. Light gray areas represent missing measurements.

flux rapidly increased when the soil moisture is high during the Asian monsoon, causing the release of large amounts of energy from the soil (Yao et al., 2011). The frequent freeze–thaw cycles occur within the active layer, and more energy is used for the ice–water phase change, decreased the soil temperature (Hu et al., 2020; Li et al., 2019). Furthermore, the errors in soil moisture are larger at the QT09 and QT13 sites compared to the other sites (Fig. 9c and e), which is consistent with the larger errors in the simulated soil temperature at these sites (Fig. 5b and d). Although STC is strongly dependent on soil moisture, it only slightly influences soil moisture. The improvements in the simulated soil moisture by the BA2005 scheme were slight, especially for the frozen period (Fig. 9). Identical results were obtained by Dai et al. (2019a), who suggested that these slight changes in soil moisture can cause notable changes in soil thermal properties. This is reflected in Fig. 9; unfrozen water content is underestimated at most sites by CLM5.0, which may produce more ice content and result in higher STC values during the frozen period. Therefore, more improvements are required in the hydrothermal process, such as unfrozen water, soil evaporation, and hydraulic conductivity, during the frozen period.

4.2.2. *The influence of soil properties*

STC strongly depends on soil properties, including the soil texture (sand, clay, and gravel), SOM, and quartz content (Farouki, 1981; He et al., 2020a; Lawrence and Slater, 2008; Yi et al., 2018). The STC scheme was originally proposed for mineral soils, and quartz content was considered in the thermal conductivity calculation of soil solids (Johansen, 1975; Kersten, 1949). Quartz content can be monitored by X-ray fluorescence and X-ray diffraction (Schonenberger et al., 2012; Tarnawski and Leong, 2012), but it is difficult to do so in practice. Generally, two main methods are used to calculate the quartz content: (i) quartz content equals sand content (Lu et al., 2007; Yang and Koike, 2005); and (ii) quartz content equals half the sand content (Balland and Arp, 2005; Chen et al., 2012; Johansen, 1975). For most areas, the first method has been shown to perform better than the second method (He et al., 2021, 2020a). Particularly, in permafrost regions, when the quartz content of STC scheme by Lu et al. (2007) was replaced by the second method, the prediction accuracy considerably improved (Du et al., 2020).

Subsequently, SOM and gravel in the soil were also incorporated into the STC scheme as they can alter the hydraulic and thermal properties of the soil (Balland and Arp, 2005; Chadburn et al., 2015; Lawrence and Slater, 2008). SOM has insulating properties and increases soil porosity (Chadburn et al., 2015; Chen et al., 2012; Lawrence and Slater, 2008; Yang et al., 2009). Some studies have revealed that the SOM content of topsoil was higher than that of the underlying soil layers over the TP (Chen et al., 2012; Yang et al., 2009, 2020). Consequently, when SOM was incorporated into the STC scheme, overestimations in soil moisture and STC were reduced (Chen et al., 2012; Lawrence and Slater, 2008). In our study, this phenomenon is also confirmed between the F1981 and LS2008 schemes (Fig. 2), wherein SOM is incorporated into the LS2008 scheme based on the F1981 scheme (Table 2). Furthermore, gravel, an indispensable part of the soil, has different thermal and hydraulic

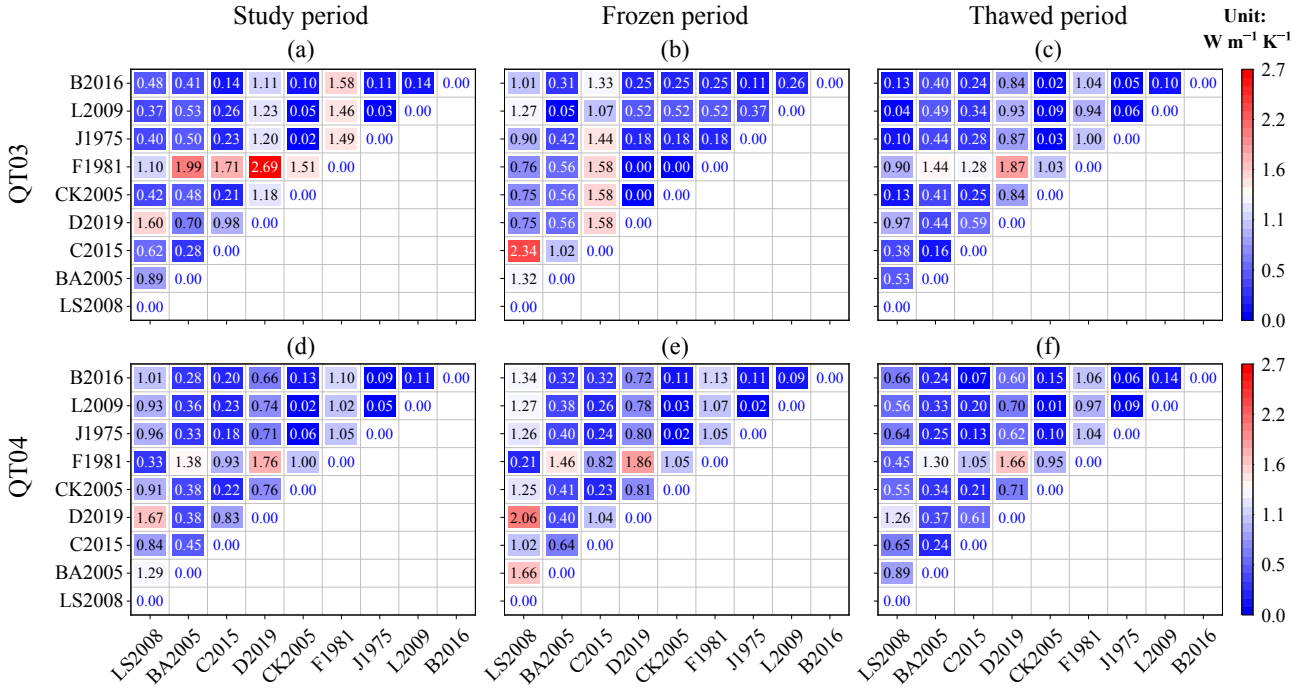

Fig. 7. The absolute value of differences in the soil thermal conductivity (STC) simulations among the nine STC schemes during different periods at a soil depth of 5 cm for the QT03 and QT04 sites.

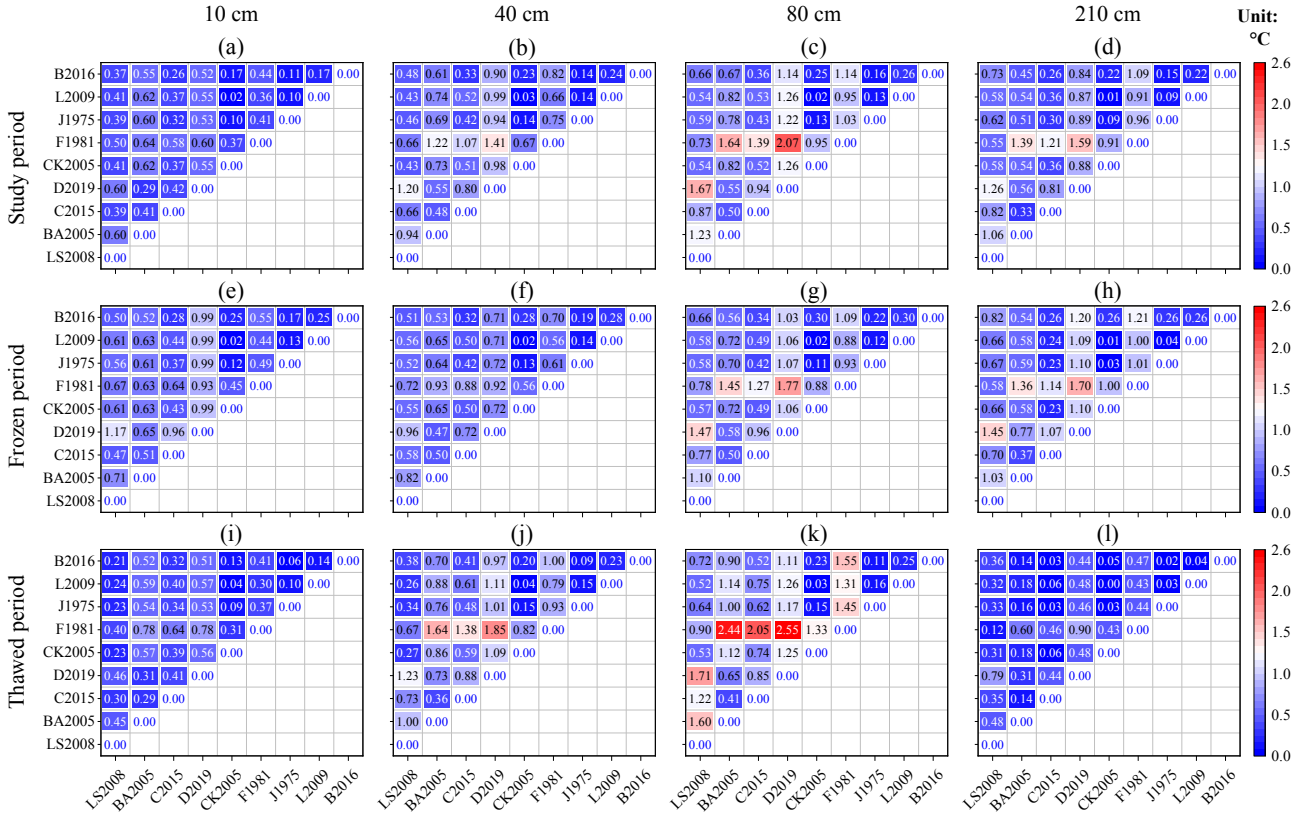

Fig. 8. The absolute value of differences in the soil temperature simulations among the nine soil thermal conductivity schemes at different soil depths during different periods at the six sites.

properties resulting from fine soils (diameter < 2 mm) (Pan et al., 2015; Yi et al., 2018), but it is generally neglected in STC schemes. Some recent studies have been conducted to incorporate gravel into the STC schemes, and they have indicated that gravel can reduce errors in simulated STC on the TP (Pan et al., 2015; Yi et al., 2018). This is similar to our results that show that the BA2005 scheme better stimulates performance in

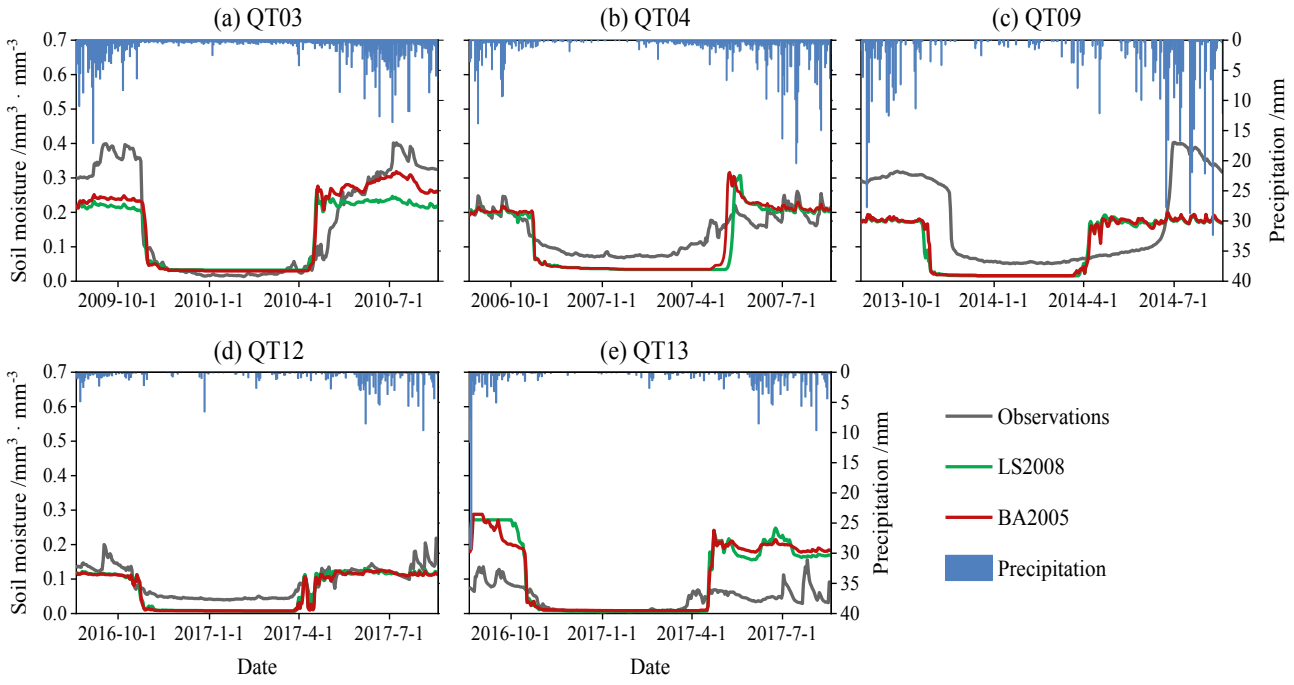

Fig. 9. Comparison of soil moisture at a soil depth of 10 cm derived from the observed (black lines) and simulated (red lines) data by the BA2005 scheme at five sites. The blue bar represents the change in precipitation.

simulated STC and soil temperature for most sites in permafrost regions on the TP than the other schemes (Figs. 3 and 6). Although the hydraulic processes were not considered in this study, it is noted that soil properties have an important influence on the hydraulic properties in LSMs, such as hydraulic conductivity and saturated soil water content (Lawrence and Slater, 2008; Dai et al., 2019b). This may further influence the soil thermal regimes (Pan et al., 2015).

4.2.3. *The influence of atmospheric forcing data*

The atmospheric forcing data play an important role in LSMs (Deng et al., 2020; Lawrence et al., 2019). Since the observed forcing data were not available for the QT12 and QT03 sites, they were replaced by the CMFD dataset. We selected the other four sites to investigate the influence of forcing data on the simulated results. Fig. 10 shows the comparison of soil temperatures using atmospheric forcing data derived from the CMFD data and observations. Differences in the simulated soil temperature between the CMFD data and observations were small at most sites. Thus, the CMFD data could be used as forcing data to drive CLM5.0 on the TP. This is consistent with other similar studies (Deng et al., 2020; Yang et al., 2018). However, the simulated accuracy is improved when the observed forcing data rather than CMFD data is used, especially for the QT03 site where the *RMSE* value is reduced by a maximum of 2.30 °C (Fig. 10a–d). Air temperature and precipitation are two key meteorological factors, and they directly determine the amount of heat and water entering the soil (Bi et al., 2016; Wang et al., 2020). Therefore, to investigate the main factors of influence, we analyzed air temperature and precipitation values derived from the CMFD data and observations at the QT03 site (Fig. 11). The figure shows that air temperature and precipitation values in the CFMD data are significantly smaller than the observed values, implying that less heat and water are entering the soil, and thus, the soil temperatures are low. However, the CMFD data has assimilated a lot of measured data, that were available in limited non-permafrost regions in China (He et al., 2020c). Hence, more monitoring networks are needed to provide reliable data on the TP, especially the permafrost regions. Furthermore, some errors remain even if the forcing data and soil textures derived from observations (Fig. 10), suggesting that additional factors may influence the simulation results, including the model structure and physical processes (Hu et al., 2020; Lawrence et al., 2019; Yang et al., 2018).

4.2.4. *Uncertainties in the model structures and other potential causes*

As analyzed in the previous section, simulated errors still exist even if the observed forcing data, soil textures, and superior STC schemes were incorporated into CLM5.0. Moreover, the soil moisture slightly improved at most sites, but was slightly worse at some sites (Fig. 9). This may be related to the model structure. CLM5.0 is a complex and highly coupled terrestrial system, and the modification of one process can often improve the simulation of other processes, but it can also expose problems in other parts of the model (Lawrence et al., 2019). Additionally, the soil temperature and moisture are affected by not only internal factors but also vegetation and other geological and climatic conditions (Bi et al., 2016; Dai et al., 2019a; Yang et al., 2020; Yue et al., 2017). For example, our results show that the nine STC schemes afforded different performances under different vegetation types (Figs. 3 and 6). The simulation errors in the soil temperatures and moisture at the QT09 site are larger than those at the other sites (Figs. 5 and 9), which may be the effect of local factors. The QT09 site is located near the north limit of permafrost regions on the TP, wherein seasonally ground soil and permafrost coexist, and the nearby landform types are more complex (Liu et al., 2020; Sun et al., 2019; Yang et al., 2020; Zhao et al., 2020). However, these spatial heterogeneities are not well reflected in the model. Furthermore, the mismatch in the spatial scales and soil stratification structures between the simulated grid cell in the model and the observed sites contributed to some errors (Chen et al., 2012; Deng et al., 2020; Yang et al., 2009).

5. Conclusions and perspectives

In this study, we evaluated the performances of nine STC schemes incorporated into CLM5.0 simulating the soil thermal properties in permafrost regions on the TP. The nine STC schemes were divided into three categories, including mineral soils, mineral and SOM soils, and mineral, SOM and gravel soils. Comprehensive statistical results showed that the mineral, SOM, and gravel soils category afforded better

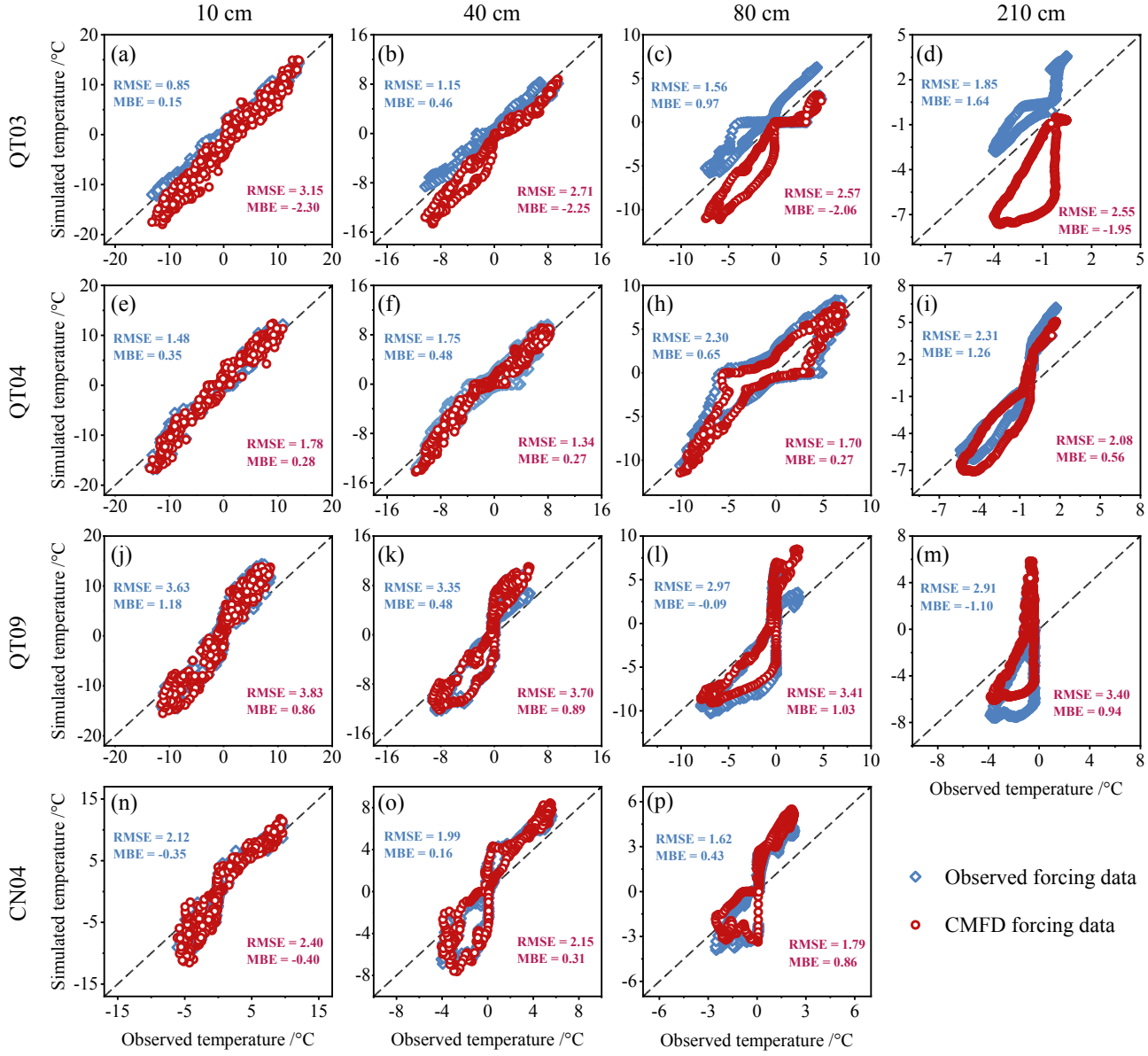

Fig. 10. Comparison of the soil temperatures simulated using the CMFD atmospheric forcing data and observations.

performance than the other categories. The BA2005 and D2019 schemes outperformed other schemes in simulating STC during the frozen period, while the LS2009 and B2016 schemes yielded better performances during the thawed period at the QT03 and QT04 sites. Moreover, the BA2005, C2015, and B2016 schemes outperformed the other schemes in simulating the soil temperature at most sites in their affiliated categories. Overall, the BA2005 schemes ranked top among the STC schemes at most sites in permafrost regions on the TP with an average RMSE decreased of 56.2% and 15.0% in simulating STC and soil temperatures compared to the default scheme (LS2008). Furthermore, the maximum differences in the simulated STC and soil temperature for the nine STC schemes incorporated into CLM5.0 were 2.69 $W \cdot m^{-1} K^{-1}$ and 2.55 °C, respectively. Additionally, all STC schemes considerably overestimated STC and underestimated soil temperature during the frozen period, except for the QT13 site. We investigated the possible causes of the simulated errors and demonstrated that soil moisture was a determining factor, which caused a large uncertainty in CLM5.0. Soil textures and atmosphere forcing data greatly influence the simulated results. Model structures, the mismatch of spatial scales, and soil stratification between the observed sites and grid cells of CLM5.0 also contributed to some errors.

Note that the applicability of different STC schemes is limited, and no single scheme can be applied to all regions. Although the performance of the BA2005 scheme at some sites was unsatisfactory, it well matched the observations at most sites. Moreover, the BA2005 scheme contained more integrated soil components, implying that it can be applied to a wide range of soil types and regions. Due to the limitations in the observation data, only six sites were used in this study. Although they spanned different typical zones and can basically reflect the characteristics of the permafrost regions on the TP, our results still exhibited some limitations when the model was applied to other regions. More observations are needed to validate and improve the parameterization schemes in the model in future studies. Additionally, although CLM5.0 has been significantly improved, its simulation of soil moisture still yields large errors, which be related to inadequate hydrological processes. Hence, more attention needs to be paid to soil's hydrological processes in LSMs, such as soil hydraulic conductivity, unfrozen water, and snow processes. Furthermore, our study is not limited to CLM5.0; the results can also be applied to other LSMs or numerical models.

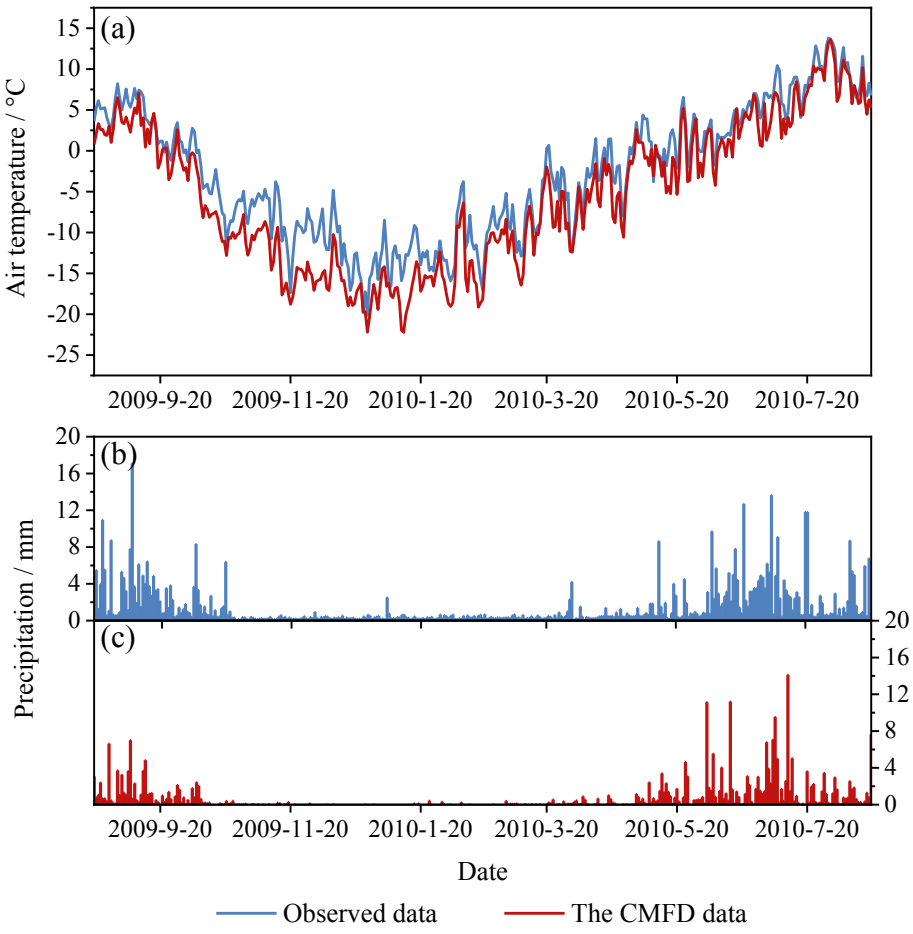

Fig. 11. Comparison of air temperature (a) and precipitation (b)-(c) derived from the observed (blue lines) and the CFMD data (red lines) at the QT03 site.

Declaration of Competing Interest

The authors declare that they have no known competing financial interests or personal relationships that could have appeared to influence the work reported in this paper.

Acknowledgments

This work is financially supported by the National Natural Science Foundation of China (42071093), the Science Fund for Innovative Research Groups of National Natural Science Foundation of China (41721091), the State Key Laboratory of Cryospheric Science (SKLCS-ZZ-2021), and the National Natural Science Foundation of China (41941015; 41690142, 41771076, 42071094; 41671070). The offline simulations are based on the scientific computing platform of the supercomputer Center of Lanzhou Branch Chinese Academy of Sciences. We would like to thank the developers of the CESM2, CMFD datasets, and China soil datasets. We also thank Dr. Zedong Liu, Xiaogang Ma, and Youqi Su for the technical assistance, and the anonymous authors for many helpful suggestions to enhance this manuscript.

Appendix A. Supplementary data

Supplementary data to this article can be found online at https://doi.org/10.1016/j.geoderma.2021.115330.

References

Balland, V., Arp, P.A., 2005. Modeling soil thermal conductivities over a wide range of conditions. J. Environ. Eng. Sci. 4 (6), 549–558. https://doi.org/10.1139/s05-007.

Bao, H., Koike, T., Yang, K., Wang, L., Shrestha, M., Lawford, P., 2016. Development of an enthalpy-based frozen soil model and its validation in a cold region in China. J. Geophys. Res.: Atmos. 121 (10), 5259–5280. https://doi.org/10.1002/2015jd024451.

Bi, H., Ma, J., Zheng, W., Zeng, J., 2016. Comparison of soil moisture in GLDAS model simulations and in situ observations over the Tibetan Plateau. J. Geophys. Res.: Atmos. 121 (6), 2658–2678. https://doi.org/10.1002/2015jd024131.

Brunke, M.A., Fairall, C.W., Zeng, X., Eymard, L., Curry, J.A., 2003. Which Bulk Aerodynamic Algorithms are Least Problematic in Computing Ocean Surface Turbulent Fluxes? J. Clim. 16 (4), 619–635. https://doi.org/10.1175/1520-0442(2003)016<0619:Wbaaal>2.0.Co;2.

Chadburn, S., Burke, E., Essery, R., Boike, J., Langer, M., Heikenfeld, M., Cox, P., Friedlingstein, P., 2015. An improved representation of physical permafrost dynamics in the JULES land-surface model. Geosci. Model Dev. 8 (5), 1493–1508. https://doi.org/10.5194/gmd-8-1493-2015.

Chen, Y., Yang, K., Tang, W., Qin, J., Zhao, L., 2012. Parameterizing soil organic carbon's impacts on soil porosity and thermal parameters for Eastern Tibet grasslands. Sci. China Earth Sci. 55 (6), 1001–1011. https://doi.org/10.1007/s11430-012-4433-0.

Cheng, G., Wu, T., 2007. Responses of permafrost to climate change and their environmental significance, Qinghai-Tibet Plateau. J. Geophys. Res. 112 (F2) https://doi.org/10.1029/2006jf000631.

Côté, J., Konrad, J.M., 2005. A generalized thermal conductivity model for soils and construction materials. Can. Geotech. J. 42 (2), 443–458. https://doi.org/10.1139/t04-106.

Dai, Y., Wei, N., Yuan, H., Zhang, S., Shangguan, W., Liu, S., Lu, X., Xin, Y., 2019a. Evaluation of Soil Thermal Conductivity Schemes for Use in Land Surface Modeling. J. Adv. Model. Earth Syst. 11 (11), 3454–3473. https://doi.org/10.1029/2019ms001723.

Dai, Y., Xin, Q., Wei, N., Zhang, Y., Shangguan, W., Yuan, H., Zhang, S., Liu, S., Lu, X., 2019b. A global high-resolution data set of soilhydraulic and thermal properties forland surface modeling. Adv. Model. Earth Syst. 11 (9), 2996–3023. https://doi.org/10.1029/2019MS001784.

de Vries, D., 1963. Thermal Properties of Soils. In: Physics of plant environment. pp: 211-234.

Deng, M., Meng, X., Lyv, Y., Zhao, L., Li, Z., Hu, Z., Jing, H., 2020. Comparison of Soil Water and Heat Transfer Modeling Over the Tibetan Plateau Using Two Community Land Surface Model (CLM) Versions. J. Adv. Model. Earth Syst. 12 (10) https://doi.org/10.1029/2020MS002189.

Ding, Y., Mu, C., Wu, T., Hu, G., Zou, D., Wang, D., Li, W., Wu, X., 2020. Increasing cryospheric hazards in a warming climate. Earth Sci. Rev. 213, 103500. https://doi.org/10.1016/j.earscirev.2020.103500.

Domine, F., Barrere, M., Sarrazin, D., 2016. Seasonal evolution of the effective thermal conductivity of the snow and the soil in high Arctic herb tundra at Bylot Island. Canada. The Cryosphere. 10 (6), 2573–2588. https://doi.org/10.5194/tc-10-2573-2016.

Du, Y., Li, R., Zhao, L., Yang, C., Wu, T., Hu, G., Xiao, Y., Zhu, X., Yang, S., Ni, J., Ma, J., 2020. Evaluation of 11 soil thermal conductivity schemes for the permafrost region of the central Qinghai-Tibet Plateau. Catena. 193, 104608. https://doi.org/10.1016/j.catena.2020.104608.

Farouki, O.T., 1981. The Thermal-Properties of Soils in Cold Regions. Cold Reg. Sci. Technol. 5 (1), 67–75. https://doi.org/10.1016/0165-232x(81)90041-0.

Farouki, O.T., 1986. Thermal properties of soils. Trans Tech Publ, Zurich, Switzerland.

Gruber, S., 2012. Derivation and analysis of a high-resolution estimate of global permafrost zonation. The Cryosphere. 6 (1), 221–233. https://doi.org/10.5194/tc-6-221-2012.

Guo, D., Wang, H., 2014. Simulated change in the near-surface soil freeze/thaw cycle on the Tibetan Plateau from 1981 to 2010. Chin. Sci. Bull. 59 (20), 2439–2448. https://doi.org/10.1007/s11434-014-0347-x.

He, H., Flerchinger, G.N., Kojima, Y., Dyck, M., Lv, J., 2021. A review and evaluation of 39 thermal conductivity models for frozen soils. Geoderma 382, 114694. https://doi.org/10.1016/j.geoderma.2020.114694.

He, H., He, D., Jin, J., Smits, K.M., Dyck, M., Wu, Q., Si, B., Lv, J., 2020a. Room for improvement: A review and evaluation of 24 soil thermal conductivity parameterization schemes commonly used in land-surface, hydrological, and soil-vegetation-atmosphere transfer models. Earth Sci. Rev. 211, 103419. https://doi.org/10.1016/j.earscirev.2020.103419.

He, H., Noborio, K., Johansen, Ø., Dyck, M., Lv, J., 2020b. Normalized concept for effective soil thermal conductivity modelling from dryness to saturation. Eur. J. Soil Sci. 71 (1), 27–43. https://doi.org/10.1111/ejss.12820.

He, H., Zhao, Y., Dyck, M.F., Si, B., Jin, H., Lv, J., Wang, J., 2017. A modified normalized model for predicting effective soil thermal conductivity. Acta Geotech. 12 (6), 1281–1300. https://doi.org/10.1007/s11440-017-0563-z.

He, J., Yang, K., Tang, W., Lu, H., Qin, J., Chen, Y., Li, X., 2020c. The first high-resolution meteorological forcing dataset for land process studies over China. Sci. Data. 7 (1), 25. https://doi.org/10.1038/s41597-020-0369-y.

Hinzman, L.D., Kane, D.L., Gieck, R.E., Everett, K.R., 1991. Hydrologic and Thermal-Properties of the Active Layer in the Alaskan Arctic. Cold Reg. Sci. Technol. 19 (2), 95–110. https://doi.org/10.1016/0165-232x(91)90001-W.

Hu, G., Zhao, L., Li, R., Wu, X., Wu, T., Xie, C., Zhu, X., Su, Y., 2019. Variations in soil temperature from 1980 to 2015 in permafrost regions on the Qinghai-Tibetan Plateau based on observed and reanalysis products. Geoderma 337, 893–905. https://doi.org/10.1016/j.geoderma.2018.10.044.

Hu, G., Zhao, L., Wu, X., Li, R., Wu, T., Xie, C., Pang, Q., Zou, D., 2017. Comparison of the thermal conductivity parameterizations for a freeze-thaw algorithm with a multi-layered soil in permafrost regions. Catena. 156, 244–251. https://doi.org/10.1016/j.catena.2017.04.011.

Hu, G., Zhao, L., Zhu, X., Wu, X., Wu, T., Li, R., Xie, C., Hao, J., 2020. Review of algorithms and parameterizations to determine unfrozen water content in frozen soil. Geoderma 368, 114277. https://doi.org/10.1016/j.geoderma.2020.114277.

Johansen, Ø., 1975. Thermal conductivity of soils. Ph.D. thesis. University of Trondheim. US Army Corps of Engineers, Cold Regions Research and Engineering Laboratory, Hanover, N. H. CRREL Draft English Translation 637, Trondheim, Norway.

Kersten, M.S., 1949. Laboratory research for the determination of the thermal properties of soils. In: DTIC Document.

Lawrence, D.M., Fisher, R.A., Koven, C.D., Oleson, K.W., Swenson, S.C., Bonan, G., Collier, N., Ghimire, B., Kampenhout, L., Kennedy, D., Kluzek, E., Lawrence, P.J., Li, F., Li, H., Lombardozzi, D., Riley, W.J., Sacks, W.J., Shi, M., Vertenstein, M., Wieder, W.R., Xu, C., Ali, A.A., Badger, A.M., Bisht, G., Broeke, M., Brunke, M.A., Burns, S.P., Buzan, J., Clark, M., Craig, A., Dahlin, K., Drewniak, B., Fisher, J.B., Flanner, M., Fox, A.M., Gentine, P., Hoffman, F., Keppel-Aleks, G., Knox, R., Kumar, S., Lenaerts, J., Leung, L.R., Lipscomb, W.H., Lu, Y., Pandey, A., Pelletier, J. D., Perket, J., Randerson, J.T., Ricciuto, D.M., Sanderson, B.M., Slater, A., Subin, Z. M., Tang, J., Thomas, R.Q., Val Martin, M., Zeng, X., 2019. The Community Land Model Version 5: Description of New Features, Benchmarking, and Impact of Forcing Uncertainty. J. Adv. Model. Earth Syst. 11 (12), 4245–4287. https://doi.org/10.1029/2018ms001583.

Lawrence, D.M., Slater, A.G., 2008. Incorporating organic soil into a global climate model. Clim. Dyn. 30 (2–3), 145–160. https://doi.org/10.1007/s00382-007-0278-1.

Li, R., Zhao, L., Ding, Y., Wu, T., Xiao, Y., Du, E., Liu, G., Qiao, Y., 2012. Temporal and spatial variations of the active layer along the Qinghai-Tibet Highway in a permafrost region. Chin. Sci. Bull. 57 (35), 4609–4616. https://doi.org/10.1007/s11434-012-5323-8.

Li, R., Zhao, L., Wu, T., Wang, Q., Ding, Y., Yao, J., Wu, X., Hu, G., Xiao, Y., Du, Y., Zhu, X., Qin, Y., Yang, S., Bai, R., Du, E., Liu, G., Zou, D., Qiao, Y., Shi, J., 2019. Soil thermal conductivity and its influencing factors at the Tanggula permafrost region on the Qinghai-Tibet Plateau. Agric. For. Meteorol. 264, 235–246. https://doi.org/10.1016/j.agrformet.2018.10.011.

Li, X., Wu, T., Zhu, X., Jiang, Y., Hu, G., Hao, J., Ni, J., Li, R., Qiao, Y., Yang, C., Ma, W., Wen, A., Ying, X., 2020. Improving the Noah-MP Model for Simulating Hydrothermal Regime of the Active Layer in the Permafrost Regions of the Qinghai-Tibet Plateau. J. Geophys. Res.: Atmos. 125 (16) https://doi.org/10.1029/2020jd032588.

Liu, G., Xie, C., Zhao, L., Xiao, Y., Wu, T., Wang, W., Liu, W., 2020. Permafrost warming near the northern limit of permafrost on the Qinghai-Tibetan Plateau during the period from 2005 to 2017: A case study in the Xidatan area. Permafrost Periglacial Processes. https://doi.org/10.1002/ppp.2089.

Lu, S., Ren, T., Gong, Y., Horton, R., 2007. An Improved Model for Predicting Soil Thermal Conductivity from Water Content at Room Temperature. Soil Sci. Soc. Am. J. 71 (1), 8–14. https://doi.org/10.2136/sssaj2006.0041.

Luo, Q., Wen, J., Hu, Z.Y., Lu, Y.Q., Yang, X.Y., 2020. Parameter Sensitivities of the Community Land Model at Two Alpine Sites in the Three-River Source Region. J. Meteorolog. Res. 34 (4), 851–864. https://doi.org/10.1007/s13351-020-9205-8.

Luo, S., Fang, X., Lyu, S., Zhang, Y., Chen, B., 2017. Improving CLM4.5 simulations of land–atmosphere exchange during freeze–thaw processes on the Tibetan Plateau. J. Meteorolog. Res. 31 (5), 916–930. https://doi.org/10.1007/s13351-017-6063-0.

Luo, S., Lv, S., Zhang, Y., Hu, Z., Ma, Y., Li, S., Shang, L., 2009. Soil thermal conductivity parameterization establishment and application in numerical scheme of central Tibetan plateau. China J. Geophys. 52 (4), 919–928 (in Chinese).

McCumber, M.C., Pielke, R.A., 1981. Simulation of the effects of surface fluxes of heat and moisture in a mesoscale numerical model: 1. Soil layer. J. Geophys. Res. 86 (C10), 9929. https://doi.org/10.1029/JC086iC10p09929.

Melton, J.R., Verseghy, D.L., Sospedra-Alfonso, R., Gruber, S., 2019. Improving permafrost physics in the coupled Canadian Land Surface Scheme (v.3.6.2) and Canadian Terrestrial Ecosystem Model (v.2.1) (CLASS-CTEM). Geosci. Model Dev. 12 (10), 4443–4467. https://doi.org/10.5194/gmd-12-4443-2019.

Mu, C., Abbott, B.W., Norris, A.J., Mu, M., Fan, C., Chen, X.u., Jia, L., Yang, R., Zhang, T., Wang, K., Peng, X., Wu, Q., Guggenberger, G., Wu, X., 2020. The status and stability of permafrost carbon on the Tibetan Plateau. Earth Sci. Rev. 211, 103433. https://doi.org/10.1016/j.earscirev.2020.103433.

Ni, J., Wu, T., Zhu, X., Hu, G., Zou, D., Wu, X., Li, R., Xie, C., Qiao, Y., Pang, Q., Hao, J., Yang, C., 2020. Simulation of the present and future projection of permafrost on the Qinghai-Tibet Plateau with statistical and machine learning models. J. Geophys. Res.: Atmos. 126 (2) https://doi.org/10.1029/2020jd033402.

Niu, G., Yang, Z., 2006. Effects of frozen soil on snowmelt runoff and soil water storage at a continental scale. J. Hydrometeor. 7, 937–952. https://doi.org/10.1175/JHM538.1.

Pan, Y., Lyu, S., Li, S., Gao, Y., Meng, X., Ao, Y., Wang, S., 2015. Simulating the role of gravel in freeze–thaw process on the Qinghai-Tibet Plateau. Theor. Appl. Clim. 127 (3–4), 1011–1022. https://doi.org/10.1007/s00704-015-1684-7.

Peters-Lidard, C.D., Blackburn, E., Liang, X., Wood, E.F., 1998. The effect of soil thermal conductivity parameterization on surface energy fluxes and temperatures. J. Atmosph. Sci. 55 (7), 1209–1224. https://doi.org/10.1175/1520-0469(1998)055<1209:Teostc>2.0.Co;2.

Qin, Y., Wu, T., Wu, X., Li, R., Xie, C., Qiao, Y., Hu, G., Zhu, X., Wang, W., Shang, W., 2017. Assessment of reanalysis soil moisture products in the permafrost regions of the central of the Qinghai-Tibet Plateau. Hydrol. Processes. 31 (26), 4647–4659. https://doi.org/10.1002/hyp.v31.2610.1002/hyp.11383.

Qiu, J., 2008. China: The third pole. Nature 454 (7203), 393–396. https://doi.org/10.1038/454393a.

Ren, T., Noborio, K., Horton, R., 1999. Measuring soil water content, electrical conductivity, and thermal properties with a Thermo-Time Domain Reflectometry Probe. Soil Sci. Soc. Am. J. 63, 450–457. https://doi.org/10.2136/sssaj1999.03615995006300030005x.

Schonenberger, J., Momose, T., Wagner, B., Leong, W.H., Tarnawski, V.R., 2012. Canadian Field Soils I. Mineral Composition by XRD/XRF Measurements. Int. J. Thermophys. 33 (2), 342–362. https://doi.org/10.1007/s10765-011-1142-4.

Shangguan, W., Dai, Y., Liu, B., Zhu, A., Duan, Q., Wu, L., Ji, D., Ye, A., Yuan, H., Zhang, Q., Chen, D., Chen, M., Chu, J., Dou, Y., Guo, J., Li, H., Li, J., Liang, L.u., Liang, X., Liu, H., Liu, S., Miao, C., Zhang, Y., 2013. A China data set of soil properties for land surface modeling. J. Adv. Model. Earth Syst. 5 (2), 212–224. https://doi.org/10.1002/jame.v5.210.1002/jame.20026.

Slusarchuk, W.A., Watson, G.H., 1975. Thermal Conductivity of Some Ice-rich Permafrost Soils. Can. Geotech. J. 12 (3), 413–424. https://doi.org/10.1139/t75-045.

Sun, Z., Zhao, L., Hu, G., Qiao, Y., Du, E., Zou, D., Xie, C., 2019. Modeling permafrost changes on the Qinghai-Tibetan plateau from 1966 to 2100: A case study from two boreholes along the Qinghai-Tibet engineering corridor. Permafrost Periglacial Processes. 31 (1), 156–171. https://doi.org/10.1002/ppp.v31.110.1002/ppp.2022.

Swenson, S.C., Lawrence, D.M., 2014. Assessing a dry surface layer-based soil resistance parameterization for the community land model using GRACE and FLUXNET-MTE data. J. Geophys. Res.: Atmos. 119 (17), 10,299–10,312. https://doi.org/10.1002/2014JD022314.

Tarnawski, V.R., Leong, W.H., 2012. A Series-Parallel Model for Estimating the Thermal Conductivity of Unsaturated Soils. Int. J. Thermophys. 33 (7), 1191–1218. https://doi.org/10.1007/s10765-012-1282-1.

Wang, A., Zeng, X., 2012. Evaluation of multireanalysis products with in situ observations over the Tibetan Plateau. J. Geophys. Res.: Atmos. 117 (D05102) https://doi.org/10.1029/2011JD016553.

Wang, Q., Li, W., Xiao, C., Ai, W., 2020. Evaluation of High-Resolution Crop Model Meteorological Forcing Datasets at Regional Scale: Air Temperature and Precipitation over Major Land Areas of China. Atmosphere. 11 (9), 1011. https://doi.org/10.3390/atmos11091011.

Wang, S., Ma, Y., 2018. On the simulation of sensible heat flux over the Tibetan Plateau using different thermal roughness length parameterization schemes. Theor. Appl. Clim. 137 (3–4), 1883–1893. https://doi.org/10.1007/s00704-018-2704-1.

Wang, Z., Wang, Q., Zhao, L., Wu, X., Yue, G., Zou, D., Nan, Z., Liu, G., Pang, Q., Fang, H., Wu, T., Shi, J., Jiao, K., Zhao, Y., Zhang, L., 2016. Mapping the vegetation distribution of the permafrost zone on the Qinghai-Tibet Plateau. J. Mountain Sci. 13 (6), 1035–1046. https://doi.org/10.1007/s11629-015-3485-y.

Wu, X., Nan, Z., Zhao, S., Zhao, L., Cheng, G., 2018. Spatial modeling of permafrost distribution and properties on the Qinghai-Tibet Plateau. Permafrost Periglacial Processes. 29 (2), 86–99. https://doi.org/10.1002/ppp.v29.210.1002/ppp.1971.

Yang, K., Chen, Y.Y., Qin, J., 2009. Some practical notes on the land surface modeling in the Tibetan Plateau. Hydrol. Earth Syst. Sci. 13 (5), 687–701. https://doi.org/10.5194/hess-13-687-2009.

Yang, K., Koike, T., 2005. Inverse analysis of the role of soil vertical heterogeneity in controlling surface soil state and energy partition. J. Geophys. Res. 110 (D8) https://doi.org/10.1029/2004jd005500.

Yang, K., Koike, T., Ishikawa, H., Kim, J., Li, X., Liu, H.Z., Liu, S.M., Ma, Y.M., Wang, J. M., 2008. Turbulent flux transfer over bare-soil surfaces: Characteristics and parameterization. J. Appl. Meteorol. Climatol. 47 (1), 276–290. https://doi.org/10.1175/2007jamc1547.1.

Yang, K., Wang, C., Li, S., 2018. Improved Simulation of Frozen-Thawing Process in Land Surface Model (CLM4.5). J. Geophys. Res.: Atmos. 123 (23) https://doi.org/10.1029/2017jd028260.

Yang, S., Li, R., Wu, T., Hu, G., Xiao, Y., Du, Y., Zhu, X., Ni, J., Ma, J., Zhang, Y., Shi, J., Qiao, Y., 2020. Evaluation of reanalysis soil temperature and soil moisture products in permafrost regions on the Qinghai-Tibetan Plateau. Geoderma 377, 114583. https://doi.org/10.1016/j.geoderma.2020.114583.

Yao, J., Zhao, L., Gu, L., Qiao, Y., Jiao, K., 2011. The surface energy budget in the permafrost region of the Tibetan Plateau. Atmos. Res. 102 (4), 394–407. https://doi.org/10.1016/j.atmosres.2011.09.001.

Yao, T., Xue, Y., Chen, D., Chen, F., Thompson, L., Cui, P., Koike, T., Lau, W.K.M., Lettenmaier, D., Mosbrugger, V., Zhang, R., Xu, B., Dozier, J., Gillespie, T., Gu, Y., Kang, S., Piao, S., Sugimoto, S., Ueno, K., Wang, L., Wang, W., Zhang, F., Sheng, Y., Guo, W., AilikunYang, X., Ma, Y., Shen, S.S.P., Su, Z., Chen, F., Liang, S., Liu, Y., Singh, V.P., Yang, K., Yang, D., Zhao, X., Qian, Y., Zhang, Y., Li, Q., 2019. Recent Third Pole's Rapid Warming Accompanies Cryospheric Melt and Water Cycle Intensification and Interactions between Monsoon and Environment: Multidisciplinary Approach with Observations, Modeling, and Analysis. Bull. Am. Meteorol. Soc. 100 (3), 423–444. https://doi.org/10.1175/bams-d-17-0057.1.

Yi, S., He, Y., Guo, X., Chen, J., Wu, Q., Qin, Y., Ding, Y., 2018. The physical properties of coarse-fragment soils and their effects on permafrost dynamics: a case study on the central Qinghai-Tibetan Plateau. The Cryosphere. 12 (9), 3067–3083. https://doi.org/10.5194/tc-12-3067-2018.

Yue, G., Zhao, L., Wang, Z., Zhang, L., Zou, D., Niu, L., Zhao, Y., Qiao, Y., 2017. Spatial Variation in Biomass and Its Relationships to Soil Properties in the Permafrost Regions Along the Qinghai-Tibet Railway. Environ. Eng. Sci. 34 (2), 130–137. https://doi.org/10.1089/ees.2014.0504.

Zhang, G., Nan, Z., Wu, X., Ji, H., Zhao, S., 2019. The Role of Winter Warming in Permafrost Change Over the Qinghai-Tibet Plateau. Geophys. Res. Lett. 46 (20), 11261–11269. https://doi.org/10.1029/2019gl084292.

Zhang, M., Pei, W., Li, S., Lu, J., Jin, L., 2017. Experimental and numerical analyses of the thermo-mechanical stability of an embankment with shady and sunny slopes in a permafrost region. Appl. Therm. Eng. 127, 1478–1487. https://doi.org/10.1016/j.applthermaleng.2017.08.074.

Zhang, X., Gao, Z., Wei, D., 2012. The sensitivity of ground surface temperature prediction to soil thermal properties Using the Simple Biosphere Model (SiB2). Adv. Atmos. Sci. 29 (3), 623–634. https://doi.org/10.1007/s00376-011-1162-9.

Zhao, L., Zou, D., Hu, G., Du, E., Pang, Q., Xiao, Y., Li, R., Sheng, Y.u., Wu, X., Sun, Z., Wang, L., Wang, C., Ma, L.u., Zhou, H., Liu, S., 2020. Changing climate and the permafrost environment on the Qinghai-Tibet (Xizang) plateau. Permafrost Periglacial Processes. 31 (3), 396–405. https://doi.org/10.1002/ppp.v31.310.1002/ppp.2056.

Zhou, X., Zhou, J., Kinzelbach, W., Stauffer, F., 2014. Simultaneous measurement of unfrozen water content and ice content in frozen soil using gamma ray attenuation and TDR, Water Resour. Res. 50 (12), 9630–9655. https://doi.org/10.1002/2014WR015640.

Zou, D., Zhao, L., Sheng, Y., Chen, J., Hu, G., Wu, T., Wu, J., Xie, C., Wu, X., Pang, Q., Wang, W., Du, E., Li, W., Liu, G., Li, J., Qin, Y., Qiao, Y., Wang, Z., Shi, J., Cheng, G., 2017. A New Map of the Permafrost Distribution on the Tibetan Plateau. The Cryosphere. https://doi.org/10.5194/tc-2016-187.